Instituto Superior
de Engenharia
Politécnico de Coimbra

DEPARTMENT OF MECHANICAL ENGINEERING

Production of Recycled Open-Cell Aluminium Foams and their Application in Electrocoagulation-based Wastewater Treatment

Dissertation to fulfil the Master's degree in Mechanical Engineering

Specialization Area of Construction and Maintenance of Mechanical Equipments

Author

Vasco Valente Oliveira Soares

Supervisor

Cândida Maria dos Santos Pereira Malça

Co-Supervisor

Sonja Jozić

INSTITUTO POLITÉCNICO
DE COIMBRA

INSTITUTO SUPERIOR
DE ENGENHARIA
DE COIMBRA

Coimbra, 03/2026

ACKNOWLEDGEMENTS

Firstly, I would like to express my sincere gratitude to my supervisor, Professor Cândida Maria dos Santos Pereira Malça, for taking me on as her student and for her motivation, support, and patience throughout this journey. Her trust, encouragement, and insightful feedback were invaluable, and I am deeply grateful for the opportunity to have learnt under her supervision.

My sincere thanks also go to Professor Sonja Jozić, whose expertise and guidance were essential during the entire foam production stage. Her technical knowledge, constructive feedback, and availability greatly enriched the experimental development of this project.

I am equally grateful to Ana Sofia Fajardo for her valuable assistance during the electrocoagulation experiments. Her support, dedication, and willingness to help were crucial to ensuring the accuracy and reliability of the experimental results.

I also acknowledge the Coimbra Institute of Engineering (ISEC), the Department of Mechanical Engineering, and the Faculty of Engineering of the University of Split (FESB) for providing the resources, facilities, and environment that made this work possible.

Finally, I would like to express my heartfelt thanks to my family, whose encouragement, patience, and unwavering support have accompanied me throughout my academic journey. Completing this dissertation marks an important milestone, and I am deeply grateful for their presence at every step of the way.

ABSTRACT

As industries seek to reduce waste and improve resource efficiency, the development of sustainable materials and circular manufacturing routes has become increasingly important. This dissertation investigates the feasibility of producing open-cell aluminium foams from recycled machining chips and assesses their potential use as sacrificial anodes in electrocoagulation (EC) wastewater treatment. Initially, eight foams were fabricated using four aluminium alloys and two space-holder salts. However, only six of these specimens demonstrated adequate structural integrity for mechanical characterisation.

Mechanical testing revealed that the replication method had successfully produced interconnected porous structures with densities ranging from 0.89 to 1.29 g/cm³. The foams exhibited progressive densification without a distinct plateau region, due to variations in pore geometry and strut thickness. Calculating energy absorption values between 5% and 60% strain revealed a strong dependency on alloy strength and pore morphology. The highest performance was observed in the Al7075–Himalayan salt foam (28.34 kJ/m³).

Electrocoagulation experiments were conducted using foams produced from Al360 and Al380, as well as two different types of salt. All samples exhibited stable electrochemical activity, achieving significant reductions in chemical oxygen demand (COD), with initial values ranging from 1670 to 2040 mg O_2/L and final values ranging from 102 to 333 mg O_2/L. The Al380 foam produced with table salt had the highest COD removal efficiency (93%) and the lowest specific energy consumption (1.51 ± 0.14 kWh/m³).

Based on the findings of this study, it can be concluded that recycled-chip aluminium foams can serve as mechanically robust and effective EC electrodes, offering a promising way to transform industrial waste into functional materials for use in sustainable wastewater treatment applications.

Keywords: Aluminium foams; Recycling; Machining chips; Space-holder method; Mechanical characterisation; Energy absorption; Electrocoagulation; Wastewater treatment; Chemical oxygen demand; Sacrificial anodes.

INDEX

List of Figures

List of Tables

LIST OF ACRONYMS AND ABBREVIATIONS

COD	Chemical Oxygen Demand
CVD	Chemical Vapour Deposition
DC	Direct Current
DSC	Differential Scanning Calorimetry
DUOCEL	Trade name for open-cell metal foam (Investment Casting Process)
EC	Electrocoagulation
E-P-P-R	Elastic-Perfectly-Plastic-Rigid model
EU	European Union
FESB	Faculty of Electrical Engineering, Mechanical Engineering, and Naval Architecture
INCO	International Nickel Company (nickel-foam CVD process)
ISEC	Coimbra Institute of Engineering
MMC	Metal Matrix Composite
NRC	Noise Reduction Coefficient
PID	Proportional–Integral–Derivative (controller)
R-P-P-L	Rigid-Perfectly-Plastic-Locking model
SD	Standard Deviation
TMA	Thermomechanical Analysis

LIST OF SYMBOLS

Latin Alphabet

a	Cross-sectional area (mm^2)
Abs	Absorbance (–)
D	Diameter (mm)
df	Dilution factor (–)
E	Young's modulus (GPa)
E_c	Energy consumption ($kWh \cdot m^{-3}$)
Ea	Absorbed acoustic energy (J)
Ei	Incident acoustic energy (J)
Er	Reflected acoustic energy (J)
Et	Transmitted acoustic energy (J)
F	Force (N)
G	Shear modulus (GPa)
HB	Brinell Hardness
HV	Vickers Hardness
HC	Heat transfer coefficient ($W \cdot m^{-2} \cdot K^{-1}$)
h	Height (mm)
I	Current intensity (A)
l	Length (mm)
pH	Potential of Hydrogen (measure of acidity or alkalinity)
q	Heat flux ($W \cdot m^{-2}$)
r	Electrical resistivity ($\Omega \cdot m$)
s	Spacing (mm)
t	Time (h)
T	Time (min)
V	Voltage (V)
v	Volume (cm^3)
W	Energy absorbed ($kJ \cdot m^{-3}$)
w	Width (mm)
x	Electrical conductivity ($mS \cdot cm^{-1}$)
ΔT	Temperature difference (°C)
°C	Degree Celsius (°C)
%	Percentage, ratio of quantity to 100

Greek Alphabet

α	Sound absorption coefficient (–)
Δ	Increment or change (–)
ε	Strain (–)
ε_{cr}	Critical strain (–)
ε_{max}	Maximum strain (–)
ε_D	Densification strain (–)
η	Loss factor (damping) (–)
ν	Poisson's ratio (–)
ϱ	Density (g/cm^3)
ϱ_0	Initial foam density (g/cm^3)
ϱ_s	Density of solid material (g/cm^3)
$\tilde{\varrho}$	Apparent density of foam (g/cm^3)
σ	Stress (MPa)
σ_{pl}	Plateau stress (MPa)
σ_t	Tensile strength (MPa)
σ_c	Compressive stress (MPa)
φ	Degree of deformation (–)
$\boldsymbol{\varphi}$	Porosity of the foam (–)
Ω	Ohms (Ω)

1 INTRODUCTION

Over the past few decades, aluminium has become one of the most strategically important engineering materials, thanks to its low density, corrosion resistance and extensive recyclability. As global demand continues to rise, increasing attention is being given to the environmental impact of producing primary aluminium and to the need to create value-added applications for recycled materials [1-4]. These concerns have encouraged the development of manufacturing processes that can transform waste aluminium into functional, high-performance materials, thereby contributing to the goals of the circular economy and sustainable engineering practices.

Among the most promising of these products are metallic foams. Their low density, interconnected porosity and high specific surface area give rise to behaviours that cannot be achieved with bulk materials. These include efficient energy absorption, high permeability and enhanced mass and heat transfer [5-6]. Open-cell foams offer superior fluid accessibility and interconnected porosity, making them ideal for use in chemical processing, acoustic, and vibration damping [7]. The space-holder method is a widely adopted fabrication route for open-cell aluminium foams and has proven to be a versatile approach for producing foams with controlled pore architecture and compatibility with recycled precursors, such as machining chips [8]. By adjusting parameters such as salt type and particle morphology, foams with distinct ligament structures and porosity levels can be produced, offering a wide design space for mechanical and functional applications.

While the general mechanical behaviour of metallic foams has been extensively researched, the mechanical behaviour of recycled open-cell foams produced from chips remains far less documented, particularly concerning how their structure influences real operating conditions. This becomes an even more relevant consideration when considering potential applications that demand both mechanical robustness and high interfacial activity.

Electrocoagulation (EC) is one such application. It is an electrochemical water treatment process in which sacrificial metallic anodes release ions that destabilise and remove pollutants. Aluminium is particularly effective in this process due to the formation of hydroxide species that have a strong affinity for organic contaminants and suspended solids [9-10]. EC systems have demonstrated high removal efficiencies for industrial effluents with elevated chemical oxygen demand (COD) while operating with comparatively simple setups and moderate energy requirements [11-12]. However, their performance depends strongly on electrode geometry, surface accessibility and dissolution behaviour [10]. This suggests that porous metallic electrodes, especially those offering large effective surface areas and

tortuous flow paths, may significantly enhance EC efficiency compared to conventional bulk plates.

Despite this potential, no comprehensive studies have evaluated whether aluminium foams produced from recycled machining chips are suitable as EC anodes, nor how their mechanical stability and internal architecture influence electrochemical behaviour. Previous work carried out at FESB successfully established procedures for producing such foams using different salt systems, while complementary studies at ISEC demonstrated the feasibility of using recycled bulk aluminium in EC applications. However, the combination of these two concepts remains unexplored.

This dissertation aims to address this specific gap. Rather than providing an exhaustive characterisation of metallic foams or an extensive review of EC theory, the objective is to determine whether recycled open-cell aluminium foams can operate effectively and reliably as EC electrodes. To this end, the study combines targeted mechanical characterisation with experimental electrocoagulation tests focusing on pH evolution, conductivity, COD removal, and energy consumption.

By linking the manufacture of aluminium foam from recycled chips with the performance of EC, this work contributes to sustainable materials engineering and demonstrates how industrial waste can be transformed into valuable technological components. The results aim to clarify not only the feasibility of these foams as electrodes, but also the influence of foam morphology, alloy, and salt type on the overall efficiency of the EC process.

2 LITERATURE REVIEW

2.1 Aluminium

Aluminium (Al) is a lightweight, corrosion-resistant metal that has become an essential material in modern engineering. Its combination of low density, high specific strength and good formability enables the creation of efficient, durable structures in fields such as aerospace, construction and marine engineering [1]. Compared to conventional materials such as steel or concrete, aluminium allows significant weight reduction, thereby improving transport efficiency and reducing loads on foundations and supporting systems [13].

One of aluminium's key advantages is its excellent extrudability, which enables complex and customised cross-sectional profiles to be fabricated. This provides engineers with design flexibility and enables multiple structural and functional features to be integrated within a single component [1]. Additionally, aluminium naturally forms a protective oxide layer that offers long-term corrosion resistance and reduces the need for maintenance or surface treatments [13].

Recent advances in aluminium processing have also helped to achieve sustainability goals by reducing energy consumption and carbon emissions throughout the production process [1]. Although its lower modulus of elasticity requires careful design to prevent buckling, aluminium's ductility and resilience ensure reliable performance under variable loading conditions. These attributes make aluminium a strategic material for innovative applications.

However, despite the many performance and design advantages offered by aluminium, concerns have been raised about the sustainability of its production due to its growing demand. Metallic materials have been the cornerstone of technological advancement for millennia. They play a critical role in sectors such as energy, construction, transportation, and safety, and the demand for structural alloys is surging. Production rates are projected to increase by up to 200% by 2050. However, this accelerated growth comes at a significant environmental cost [14]. The annual production of approximately 2 billion tonnes of metals and alloys contributes to 40% of global industrial greenhouse gas emissions, consumes 10% of the world's energy resources, and necessitates the extraction of 3.2 billion tonnes of minerals. The energy-intensive processes involved in their extraction and manufacturing further exacerbate pollution, underscoring the urgent need for sustainable solutions within the metals industry [2].

Aluminium ranks as the second most consumed metal globally and leads the category of non-ferrous alloys due to its exceptional properties, including high electrical and thermal conductivity, low density, moderate strength, and remarkable ductility. Annually, aluminium consumption ranges between 60 and 80 Megatonnes

(Figure 1-(a)), with only 25% of this demand met by recycled scrap metal, highlighting the challenges associated with recycling processes [3].

Despite its widespread use, aluminium and its alloys are associated with significant environmental impacts. They represent the second most critical metal group in terms of production volume, greenhouse gas emissions, electricity demand for primary synthesis via electrolysis, and the generation of harmful by-products such as red mud. Aluminium production is particularly energy-intensive, with a global average CO_2 emission intensity of around 14.4 tonnes per tonne of metal produced, as seen in Table 1. Global annual CO_2 emissions from primary aluminium production are estimated at around 1.0 gigatonne per year (Figure 1-(b)). However, these values can vary depending on the regional energy mix, with substantially higher emissions in regions dependent on fossil fuels and lower values in areas utilising renewable energy sources, such as hydropower, for electrolysis plants. A substantial portion of these emissions is indirect, originating from the electricity consumed during the electrolysis process. These challenges underscore the need for innovative approaches to improve the sustainability of aluminium production and recycling [4] [15-16].

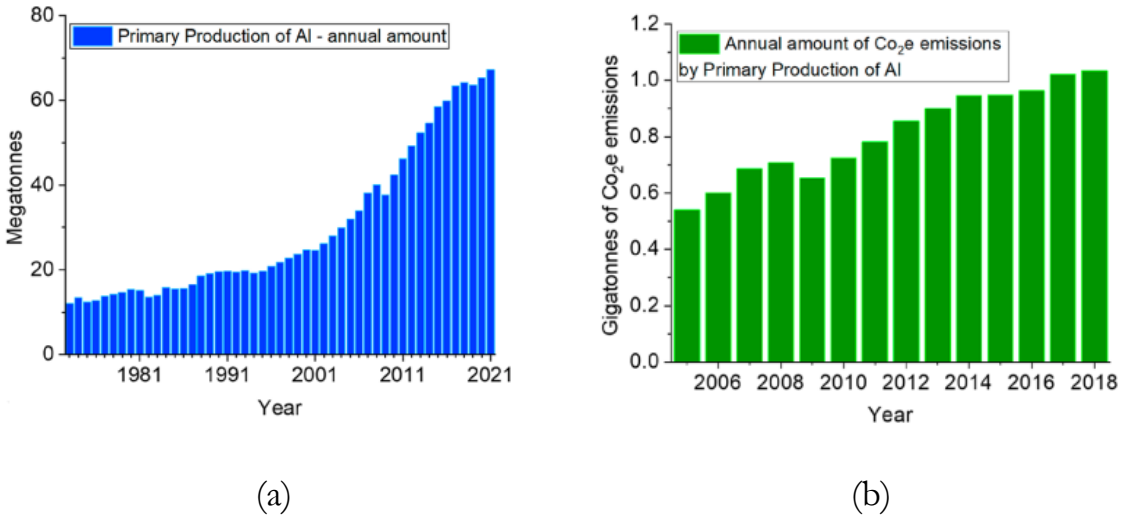

Figure 2.1 - (a) Global amount of primary aluminium production in megatonnes (Mt) for the years 1973−2021. (b) Calculated global annual amount of CO2 emissions emitted by primary production of aluminium in gigatonnes (Gt) for the years 2005−2018 [16].

Table 2.1 - Carbon Footprint of Important Materials in Comparison: Magnitude of Emissions for Several Important Material Classes [15].

Material	**Global CO_2 emissions associated with production in 2017 (Gt CO_2 per year)**	**Current global average specific CO_2 intensity (tonne CO_2 per tonne of metal produced)**
Steel	3.7	2.00
Aluminium	1.0	14.40
Nickel, cobalt	0.01	20.00
Petrochemicals	1.5	1.70
Cement	2.2	0.86

Considering the environmental challenges associated with aluminium production and recycling, this section explores alternative strategies for making use of aluminium machining chips, as illustrated in Figure 2. Powder metallurgy is a promising approach to sustainable aluminium recycling, offering efficient material recovery while minimising energy consumption. Machining chips are usually considered difficult to recycle because of their small size, high surface-to-volume ratio, and tendency to oxidise. However, they can be transformed into valuable precursors for metal foam production [17].

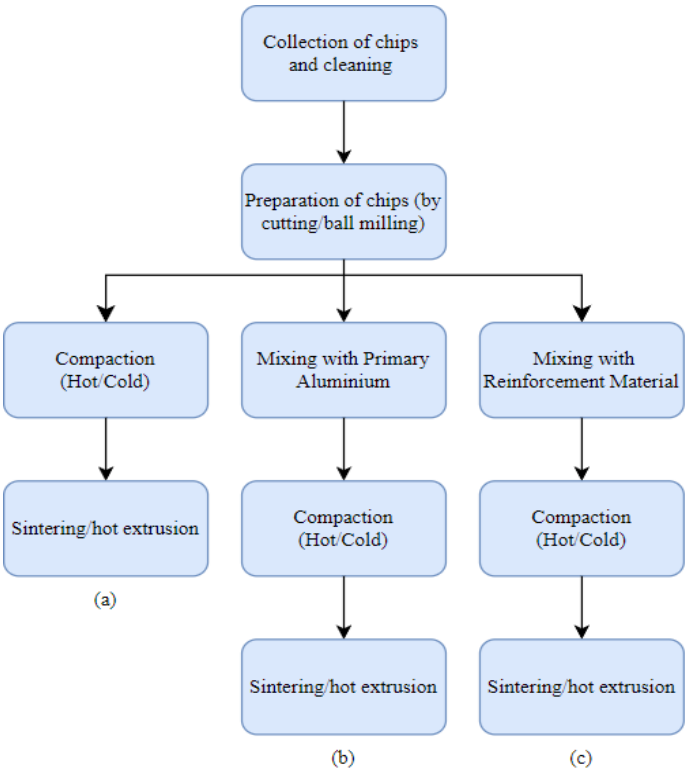

Figure 2.2 - Flow chart for the recycling of scrap aluminium: a) without reinforcement and primary aluminium; b) with primary aluminium; c) with added reinforcements [3].

2.2 Metal foams

2.2.1 Historical Remarks

The development of metal foams can be traced back to the 1940s, with a marked increase in patent registrations from the late 1950s to the 1970s. During this period, numerous variations of foaming techniques were proposed, although few details were published beyond the patent documentation, making it challenging to verify the success of these early methods. In the late 1980s, renewed scientific interest revived some of these original techniques, which led to a substantial increase in research publications [5].

Since then, advances in material science and manufacturing technology have propelled metal foams from a largely experimental phase to broader commercial applications. Recent innovations have improved the consistency and scalability of foam production, enabling better control over pore structure and mechanical properties. Modern metal foams now play a crucial role in applications ranging from energy absorbers to heat exchangers and biomedical implants. This expansion reflects the material's capacity to meet specific demands across industries, and research continues to explore new functionalities and performance enhancements.

2.2.2 Definitions

In materials science, the term "foam" traditionally describes a dispersion of gas bubbles within a liquid. By allowing this liquid foam to solidify, a "solid foam" structure is obtained, which is the typical structure referred to when discussing "metallic foams". During production, the liquid foam state is transient, only existing as a stage in the fabrication of solid cellular materials. Solid foams belong to the broader category of "cellular solids", where their morphology is influenced by the liquid phase's tendency to minimize surface energy, resulting in structures that resemble their liquid form. Unlike solid foams, cellular solids can also be produced without a liquid phase, enabling a wider range of morphologies, such as the open structure found in sintered powders. Although these porous structures are commonly referred to as 'foams', they might be more accurately described as 'sponges'. Scientific attempts to improve foam quality focus on foam physics, i.e., bubble formation, nucleation, growth, stability, development, and gas diffusion in the liquid state, where the foam structure evolves [6].

Cellular structures are kinds of porous materials resulting in high-strength, low-weight features [18]. We are familiar with natural cellular structures such as wood, cork, and bone. These are natural materials that are structured hierarchically. In engineering, man-made cellular materials (porous construction materials, cellular polymers, or ceramics) have been used for a long time because of their remarkable thermal insulation [19].

Metallic foams have characteristics that polymers, metals, ceramics, or polymer and ceramic foams do not possess; these include mechanical strength, stiffness, energy and acoustic absorption, thermal and electrical conductivity, lightweight structure, thermal control, and stability under extreme conditions [20].

2.2.3 Open Cell and Closed Cell Metallic Foams

Building on the foundational characteristics of metallic foams, these materials can be classified into open-cell and closed-cell structures, each offering unique mechanical behaviour suited to different industrial applications. The two types of cells are shown in Table 2 [20].

Open-cell foams have a complex microstructure consisting of an interconnected network of ligaments that form along the edges of randomly packed cells that evolve during the foaming process. The network of interconnected struts creates (Figure 3-(a)) a structure that permits fluid or gas permeability, making it ideal for applications such as heat exchangers and battery electrodes, where the ease of flow through the foam is beneficial. This morphology allows for deformation primarily through bending, with additional stretching and compression along the cell edges.

In contrast, closed-cell foams consist of enclosed cells separated by solid walls (Figure 3-(b)), which increases structural rigidity and provides superior load-bearing properties. The presence of cell walls introduces membrane stresses, which contribute to a higher Young's modulus in comparison to open-cell foams of similar density, making closed-cell structures especially useful for applications requiring energy absorption, such as protective padding and vibration damping in automotive and aerospace sectors.

Table 2.2 - Classification of metallic foams, open-cell vs closed-cell [20].

Open Cell	Closed Cell
Cells are complex and interconnected, making it difficult to distinguish between them.	Cell faces and cell edges are clearly defined and not interconnected.
Possesses a lower density.	Possesses a higher density.
Possesses high porosity and is lightweight.	Exhibits high energy and crash absorption.
Under mechanical loading, it exhibits lower strength.	Under mechanical loading, it exhibits high compressive strength.
Mostly used as heat exchangers, filters, and catalyst carriers.	Mostly used in energy/impact absorption, vibration control, and mechanical damping.

Ongoing research is directed toward optimizing these materials by enhancing the homogeneity of cell sizes and improving the correlation between cell structure and mechanical strength. These efforts are focused on refining manufacturing processes

and developing predictive models that can reliably simulate the mechanical behaviour of these cellular materials under various conditions [21].

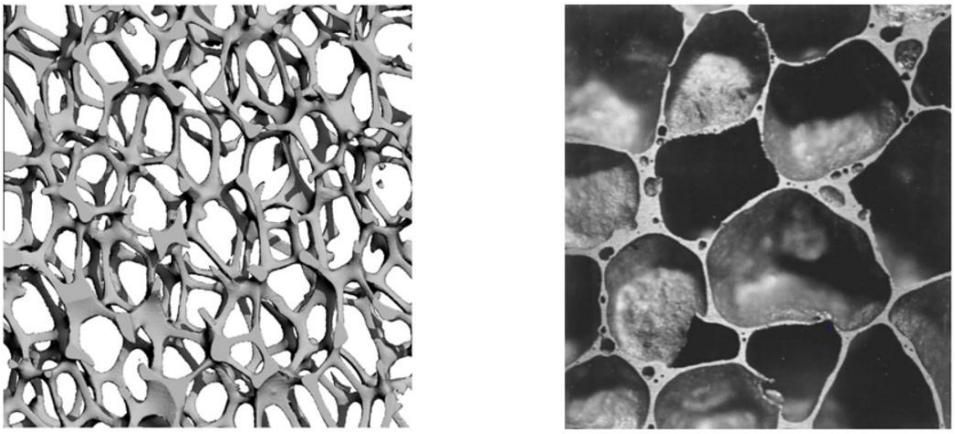

(a) (b)

Figure 2.3 - (a) Open-cell [22]. (b) Closed-cell [23].

Both of this type of cells has subtypes defined by their unique manufacturing processes, Figure 4 illustrates the relationship between cell size (in centimetres) and relative density for various manufacturing techniques used to produce both open-cell and closed-cell metal foams, this visualization supports the selection of an appropriate manufacturing method, which directly impacts the mechanical properties and functionality of the resulting metal foam [24].

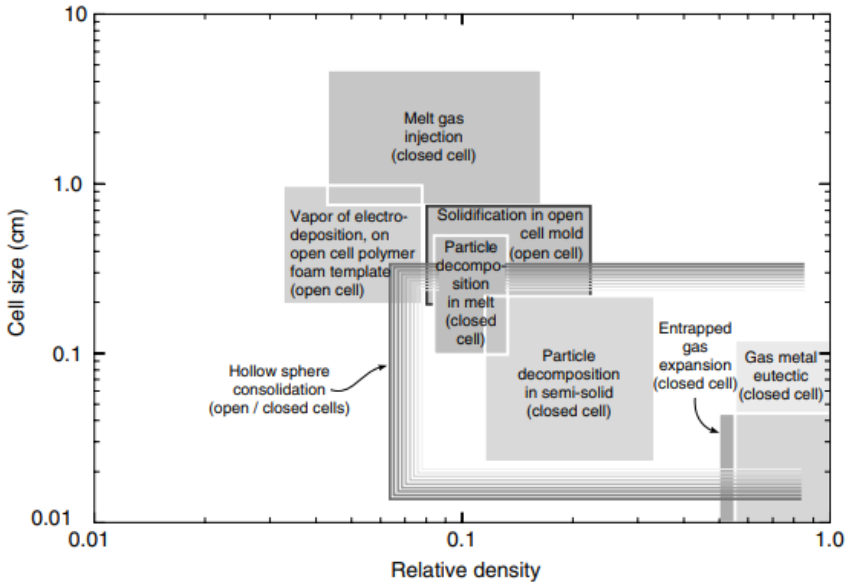

Figure 2.4 - The range of cell size and relative density for the different metals [24].

2.2.4 Production techniques

2.2.4.1 Space-Holder Technique (Open-Cell)

Despite not being commercial, this production technique was used in this study. Some differences will be explained in more detail in the experimental chapter.

The space-holder technique follows a method similar to the one shown in Figure 5. Initially, aluminium is thoroughly mixed with NaCl, ensuring uniform distribution of the space holder. The mixture is then compacted using a hydraulic press, forming a solid precursor. After compaction, the sample is immersed in boiling water to dissolve the NaCl, leaving behind a porous aluminium structure [25].

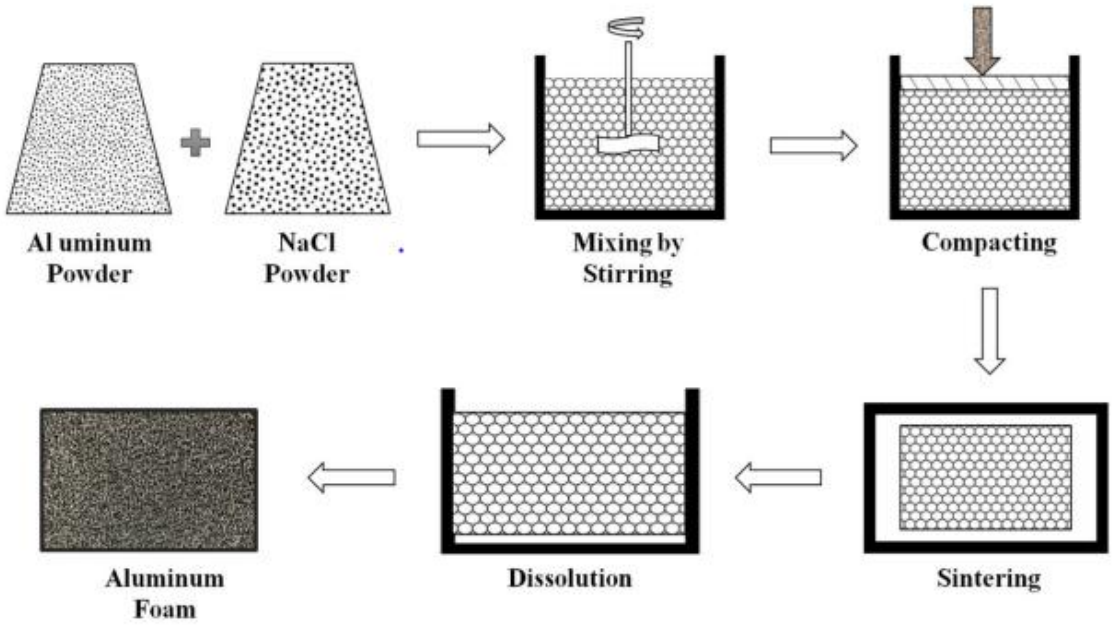

Figure 2.5 - Manufacturing of aluminium foams by using NaCl as a space holder [25].

As illustrated in Figure 6, the results of the samples of this method were observed during different stages of the process: sintering (a), machining (b), and leaching (c). The sintering process was carried out in a pre-heated electric furnace at temperatures ranging from 650°C to 700°C, which is slightly below the melting point of aluminium (660°C). During sintering, the aluminium transitions into a semi-liquid state, allowing its viscosity to be sufficient to fill the spaces between NaCl particles, forming a solid yet porous structure [8].

The salt dissolution occurs in two distinct stages. Initially, the sintered specimens are placed in a continuously running hot water bath to leach out the majority of the embedded NaCl particles. Following this, the samples are immersed in an ultrasonic washer to ensure the complete removal of any remaining salt, leaving behind a fully porous metallic foam structure [8].

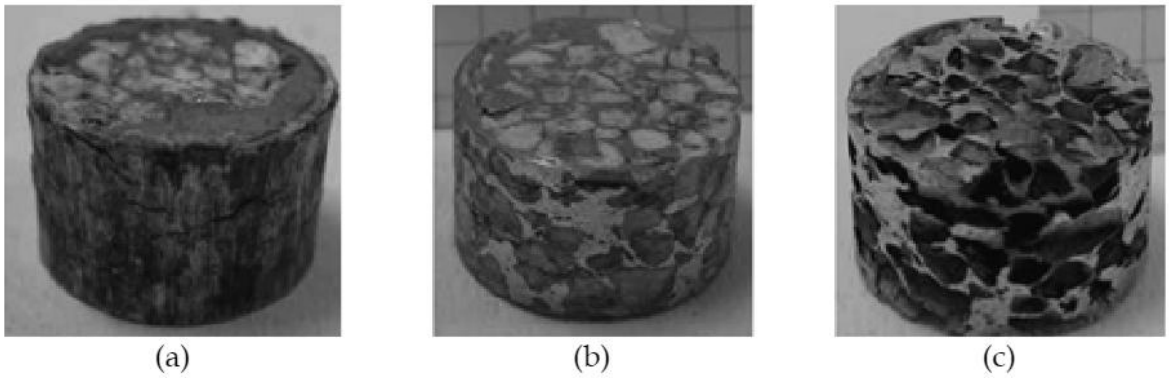

Figure 2.6 - Sample after: sintering (a), machining (b), leaching (c) [26].

The use of NaCl as a space holder offers several advantages, including its low cost, availability, and chemical stability during compaction. Additionally, NaCl's high solubility in water allows for efficient and environmentally friendly removal. However, careful control of the particle size and distribution of NaCl is critical, as these factors directly influence the final pore structure and mechanical properties of the foam. It is important to note that other space-holder materials can be used in place of NaCl.

The following subchapters provide examples of metal foam of commercial production techniques.

2.2.4.2 Melt gas injection (Closed-Cell)

Melt gas injection is one of the most widely utilized techniques for producing metallic foams, particularly aluminium-based foams. This method involves injecting a gas directly into a molten metal to create a foam structure. However, pure liquid metals do not readily foam under gas injection due to rapid drainage of the liquid phase along bubble walls, leading to instability. To counteract this, the viscosity of the melt is increased by introducing fine, insoluble ceramic particles, such as silicon carbide (SiC), aluminium oxide (Al2O3), or magnesium oxide (MgO), which impede drainage and stabilize the foam structure [24] [27].

In a typical process, aluminium or an aluminium alloy is melted, and 10–30% of the volume is made up of stabilizing ceramic particles. These particles, typically ranging from 0.5 to 25 μm in size, enhance the viscosity of the molten metal and improve foam stability. A variety of gases, including air, nitrogen, argon, carbon dioxide, and even water vapor, can be injected into the melt through specialized rotating impellers or vibrating nozzles. These mechanisms generate fine gas bubbles that are uniformly distributed throughout the melt. The foam rises to the surface, where it partially drains, leading to the formation of a relatively dry, semi-solid foam structure before solidification [24] [28].

The stability of the foam is highly dependent on the thermal gradient within the molten metal, which influences the drainage rate and the final foam morphology. Careful control of the gas injection process and cooling rate allows to production of

low-density, closed-cell foams with relative densities ranging from 0.03 to 0.1. The pore sizes typically range from 5 to 20 mm in diameter, depending on processing conditions. To extract the foam, various methods can be employed, such as drawing it off the liquid surface using conveyor belts. The solidified foam can be used in its as-cast form or cut into specific shapes as required [24]. This production technique can be seen in Figure 7.

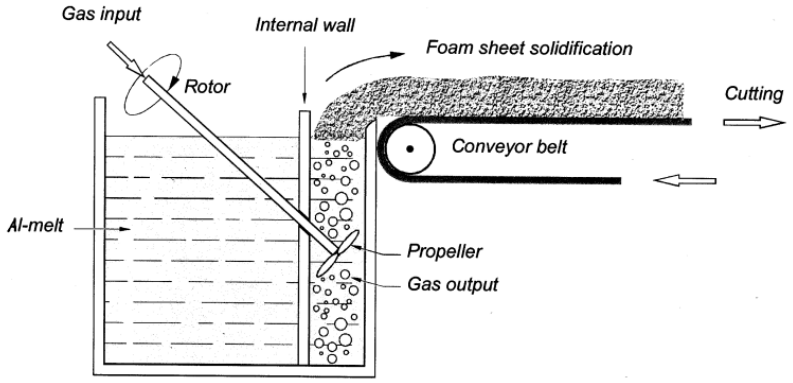

Figure 2.7 - Direct foaming of melts by gas injection (MMC foams) [6].

2.2.4.3 Blowing agent as gas source, direct foaming (Closed-Cell)

An alternative to the direct foaming of melt using an external gas source is the addition of a blowing agent to a viscous melt, which decomposes upon heating, releasing gas and initiating the foaming process. This technique, commercially exploited by Shinko Wire (Japan), requires enhancing the melt viscosity, which can be achieved by adding additives such as calcium, ceramic reinforcements, aluminium dross, and metallic viscosity-enhancing agents like manganese dioxide. This process is illustrated in Figure 8 [29].

One common method involves the addition of calcium to an aluminium alloy, followed by stirring in the presence of air to create solid particles in-situ. Subsequently, TiH2 powder is introduced, triggering gas evolution and initiating foam formation. Titanium hydride decomposes at temperatures above approximately 465°C, releasing hydrogen gas and creating bubbles that form a closed-cell foam structure if the foam drainage is sufficiently slow, requiring a high melt viscosity [30].

The amount of calcium and TiH2 added directly influences the relative density and cell size of the foam, with cell sizes ranging from 0.5 to 5 mm, depending on the TiH2 content and processing conditions. Alporas foam primarily consists of closed cells, but post-processing techniques such as rolling can be used to fracture the cell walls and enhance acoustic damping. While this batch process is more expensive than gas-injection methods, it is currently only applied to aluminium alloys due to the embrittling effects of hydrogen on other metals [30].

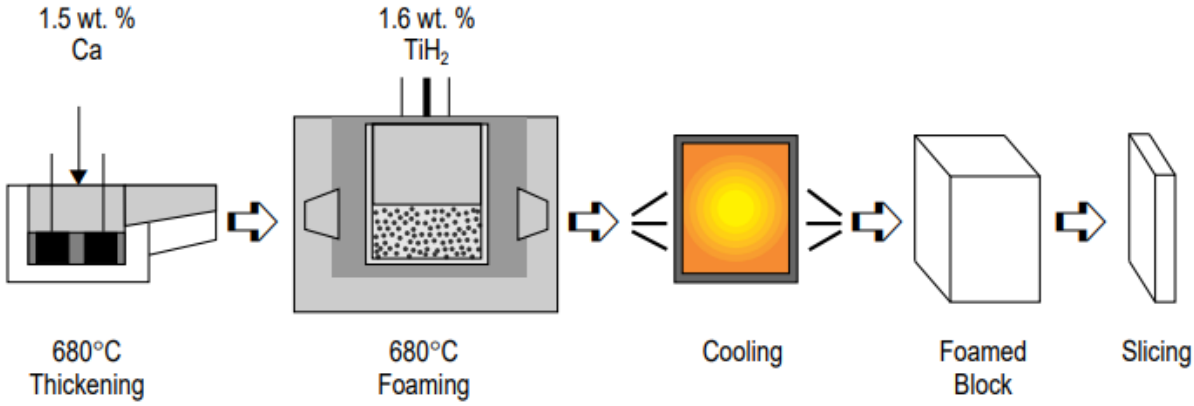

Figure 2.8 - Processing steps involved in liquid melt foaming with the addition of a blowing agent [29].

2.2.4.4 Gas-releasing particle decomposition in semi-solids for closed-cell foams

Foamed metals can be produced by a powder metallurgical method invented and patented at the Fraunhofer-Institute in Bremen [31]. The production of foamed metals involves a powder metallurgy method where a foaming agent, typically titanium hydride (TiH2), is mixed with aluminium alloy powder. TiH2 decomposes at around 465°C, below the melting point of aluminium (660°C), releasing gas that causes bubble formation and allows for partial melting of the metal. The mixture is then compacted, extruded, and heated in a sealed mold just above the alloy's solidus temperature. As the gas is released, the aluminium expands into foam, filling the mold. The process is illustrated in Figure 9. The foam stabilizes upon cooling, resulting in closed-cell foam with a relative density as low as 0.08 and cell sizes ranging from 1 to 5 mm [32]. This method has been applied to aluminium and has potential for other materials, depending on the foaming agent and process parameters.

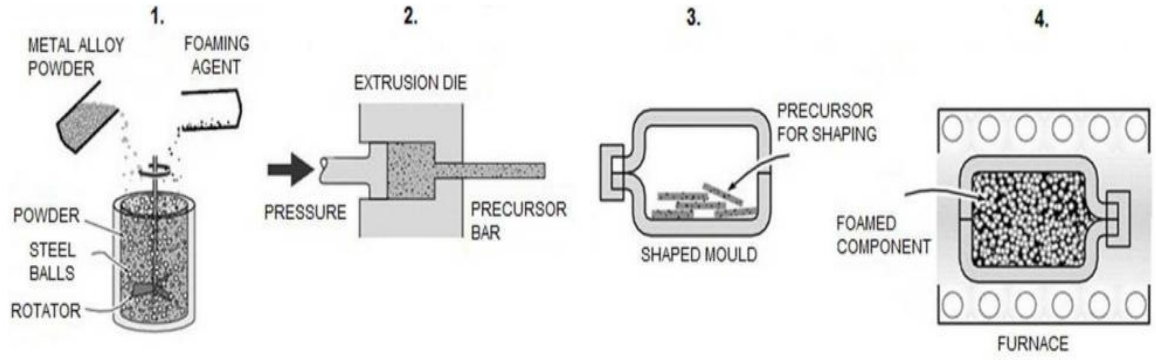

Figure 2.9 - The sequence of powder metallurgy process used for gas-releasing particles decomposition in semi-solids: 1. Selecting and mixing of the ingredients, 2. Consolidation and extrusion of precursor bars 3. Mold preparation 4. Foaming in furnace [32].

2.2.4.5 Casting technique for foam open-cell foams

The casting technique, also known as infiltration casting, is a well-established method for producing open-cell metal foams with high structural uniformity. This process involves the use of an open-cell polymer foam template, which is coated with a ceramic slurry, dried, and baked to create a rigid mold. The high-temperature treatment not only hardens the mold but also decomposes the polymer, leaving a negative replica of the foam structure [24] [33-35].

Once the mold is prepared, molten metal is introduced, often under moderate to high pressure to ensure complete infiltration, especially for alloys with high viscosity. After solidification, the mold material is removed using chemical dissolution or mechanical processes, revealing a metallic foam that replicates the morphology of the original polymer template [33-34]. Figure 10 illustrates the step-by-step process of this technique.

This method allows the production of metal foams with controlled pore sizes, typically ranging from 1 to 5 mm, and relative densities as low as 0.05. A variation of this technique involves using injection-molded polymer or wax lattices instead of polymer foams. These are coated, fired, and subsequently filled with metal using conventional investment casting techniques [34].

Despite its complexity and cost, this technique is preferred when high precision and uniformity in porosity are required. As a result, it is widely used in applications such as heat exchangers, electrodes, and filtration systems, where controlled permeability and mechanical stability are essential.

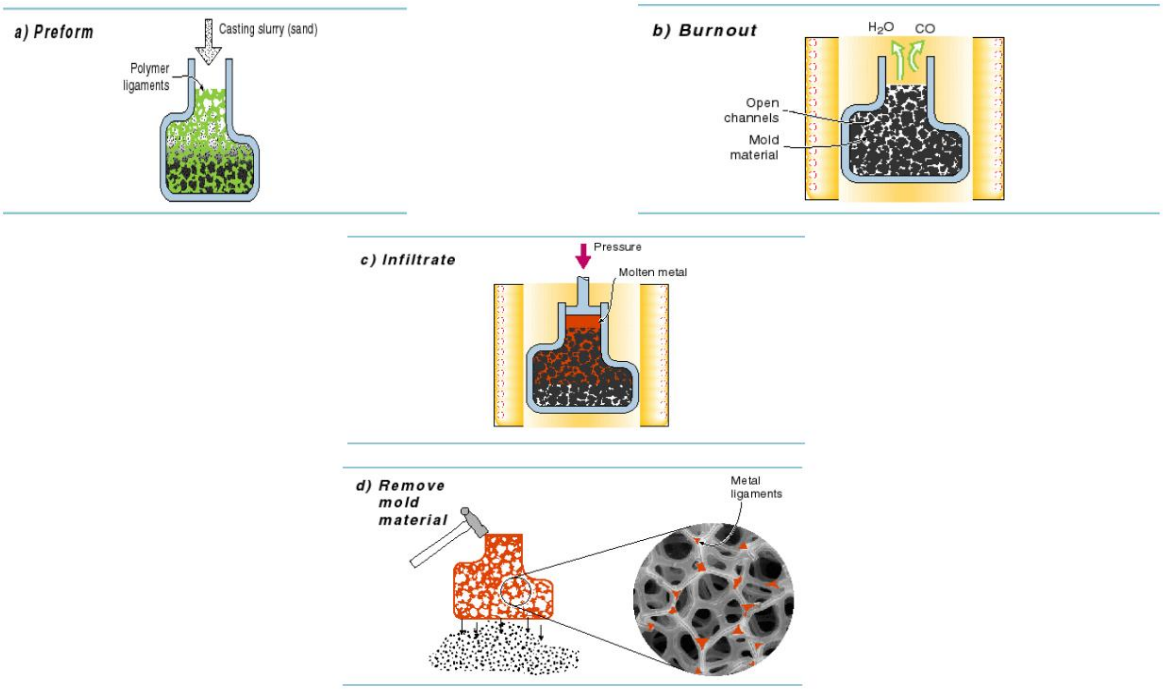

Figure 2.10 - Investment casting method to manufacture open cell foams (DUOCEL process) [33].

2.2.4.6 Metal deposition on cellular preforms (Open-Cell)

Metal deposition onto cellular preforms is a versatile method of fabricating ultralight metal foams with well-controlled pore architecture. In this process, an open-cell polymer foam (typically polyurethane) is placed inside a chemical vapour deposition (CVD) reactor, where it is uniformly coated with metal via the decomposition of a gaseous precursor. Figure 11 illustrates the three main stages of the INCO process for producing nickel foams.

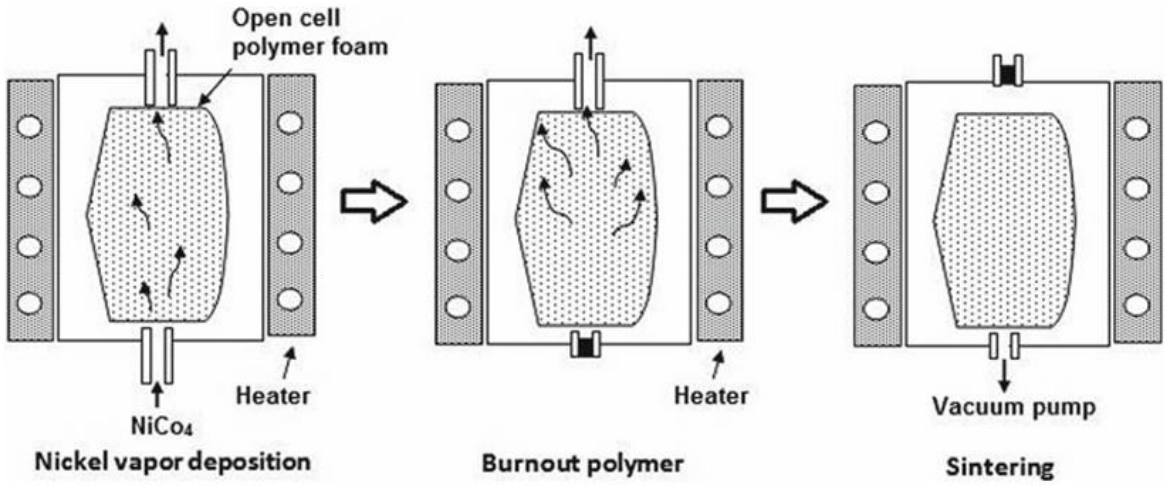

Figure 2.11 - CVD process to create open-cell nickel foam (INCO process) [36].

In the INCO CVD approach, nickel carbonyl ($Ni(CO)_4$) is introduced at around 100 °C, where it thermally decomposes on the heated foam surfaces, depositing a conformal nickel layer tens of micrometres thick while releasing carbon monoxide [24]. Infrared or radio-frequency heating can be localized to the polymer template to ensure efficient deposition without affecting the reactor walls.

Once the desired coating thickness is achieved, the metal coated preform is removed and heated in air to burn out the polymer, yielding a free-standing cellular metal structure with hollow ligaments [24][36]. A final sintering step densifies these ligaments, improving mechanical integrity and electrical conductivity.

This CVD based route produces some of the lowest relative-density metal foams available (0.02–0.05) and enables pore diameters from 100 μm up to 300 μm by selecting the initial polymer template morphology [24][36]. However, it is limited to pure metals like nickel or titanium, because co-deposition of alloys via CVD or electrodeposition remains challenging. Moreover, nickel carbonyl is highly toxic and subject to stringent environmental regulations, requiring costly abatement systems or being banned in several countries, including the United States [24][36].

2.2.5 Properties

2.2.5.1 Mechanical Properties

Before delving into the review of the mechanical properties, it is important to highlight the work of Ashby [30], who, by drawing comparisons with other porous materials, established a framework for analysing metal foams' characteristics and properties based on two sets of parameters. The first set pertains to the foam's geometric structure, including its relative density, porosity, cell size, and morphology. The second set is associated with the intrinsic properties of the cell wall material. Key parameters such as Young's modulus, density, plastic deformation behaviour, and fracture strength are particularly relevant in defining the mechanical performance of metal foams [24].

Some approximate mathematical relations for the mechanical properties of metal foams have been presented in the past and are also highlighted in Table 3 [24]:

Table 2.3 - Mechanical properties of metal foams [24].

	Open-cell Foams	**Closed-cell Foams**
Young's modulus, E (GPa)	$E = (0.1-4)E_s\left(\frac{\rho}{\rho_s}\right)^2$	$E = (0.1-1)E_s \times \left[0.5\left(\frac{\rho}{\rho_s}\right)^2 + 0.3\left(\frac{\rho}{\rho_s}\right)\right]$
Shear modulus, G (GPa)	$G \approx \frac{3}{8}E$	$G \approx \frac{3}{8}E$
Bulk modulus, K (GPa)	$K \approx 1.1E$	$K \approx 1.1E$
Poisson's ratio, v	$0.32 - 0.34$	$0.32 - 0.34$
Compressive strength, σc (MPa)	$\sigma_c = (0.1-1)\sigma_{c,s}\left(\frac{\rho}{\rho_s}\right)^{3/2}$	$\sigma_c = (0.1-1)\sigma_{c,s} \times \left[0.5\left(\frac{\rho}{\rho_s}\right)^{\frac{2}{3}} + 0.3\left(\frac{\rho}{\rho_s}\right)\right]$
Tensile strength, σt (MPa)	$\sigma_t \approx (1.1-1.4)\sigma_c$	$\sigma_t \approx (1.1-1.4)\sigma_c$

The underlying principles that influence cellular properties are common to all three classes. Three factors dominate (Figure 12):

- the properties of the solid of which the foam is made;
- the topology (connectivity) and shape of the cell edges and faces;
- the relative density, $\tilde{\rho}/\rho_s$, of the foam, where $\tilde{\rho}$ is the density of the foam and ρ_s that of the solid of which it is made [37].

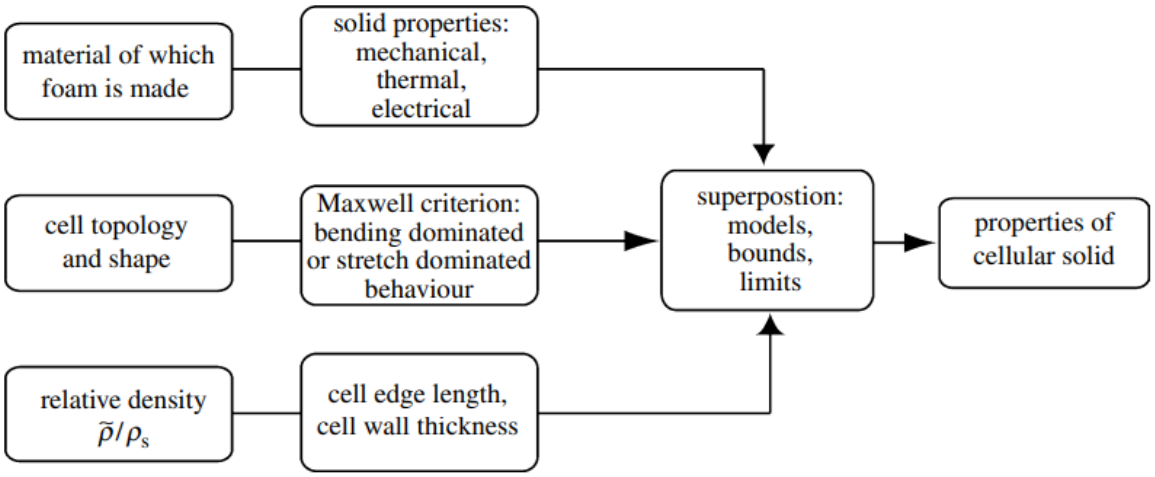

Figure 2.12 - The properties of cellular materials depend on the material of the cell walls, the cell topology, and the relative density [37].

Metal foams are widely recognized for their superior energy absorption capabilities, making them ideal for crash protection and impact mitigation. Their non-linear large deformation behaviour plays a crucial role in their ability to absorb impact energy and attenuate shock loads [38]. The energy absorption behaviour of metal foams is closely linked to the dynamic propagation of the collapsing wave, making it essential to study their collapse mechanisms experimentally. Previous research has also highlighted that shock wave propagation is crucial in all high-velocity impact regimes, influencing the extent of densification and energy dissipation [39]. Additionally, a detailed investigation into the effect of strain rate on deformation patterns reveals that foam compression follows a non-linear, large deformation process similar to other cellular materials such as honeycombs and natural composites [39].

One of the key ways to understand the behaviour of metal foams is to observe how they respond to compressive loads. This response can be characterised by three distinct deformation regions: an initial elastic region, a plateau region, and a final densification region. In this final region, the stiffness of the material increases significantly as it approaches the density of the base metal [38]. The graph in Figure 11 can be used to calculate the absorption energy from the beginning of the elastic region to the densification region.

Under quasi-static loading conditions, metal foams exhibit a characteristic stress-strain curve, as shown in Figures 13 and 14. Initially, the material undergoes elastic deformation, during which the cell walls bend without permanent deformation. As the applied load increases, the bending moment in the cell walls reaches the fully plastic moment, leading to plastic collapse. This transition results in a stress plateau, which defines the plastic collapse stress of the foam [40]. The stress and strain at the transition from the elastic to the plastic plateau region are identified as the critical

stress (σ_{cr}) and critical strain (ε_{cr}), determined by the intersection of tangents to these regions [41].

The mechanical behaviour of metal foams has been modelled using various idealisations. One widely used model is the rigid-perfectly-plastic-locking (R-P-P-L) approximation, which assumes that, once the plastic collapse stress has been reached, the material deforms at a constant stress until densification occurs. Another approach, the elastic-perfectly-plastic-rigid (E-P-P-R) model, considers the foam as fully densified at the maximum strain, $\varepsilon_{max} = (1 - \rho_0/\rho_s)$, where ρ_0 is the initial foam density, and ρ_s is the density of the solid constituent material. While the E-P-P-R model is conservative in terms of strain-energy density under compression, it predicts higher critical stress and strain values than the quasi-static experimental results as depicted in Figure 14 [38].

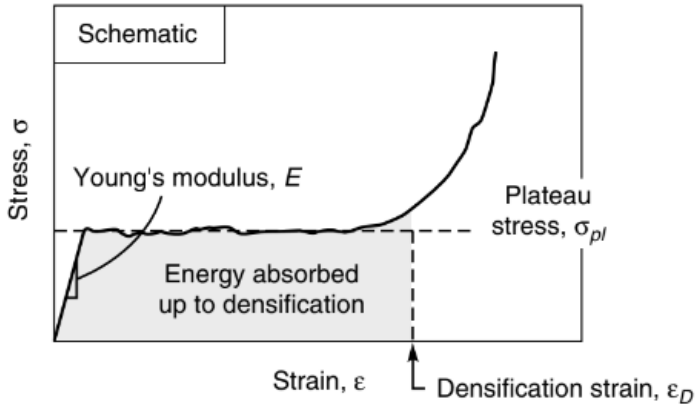

Figure 2.13 - Compression curve for a metal foam [24].

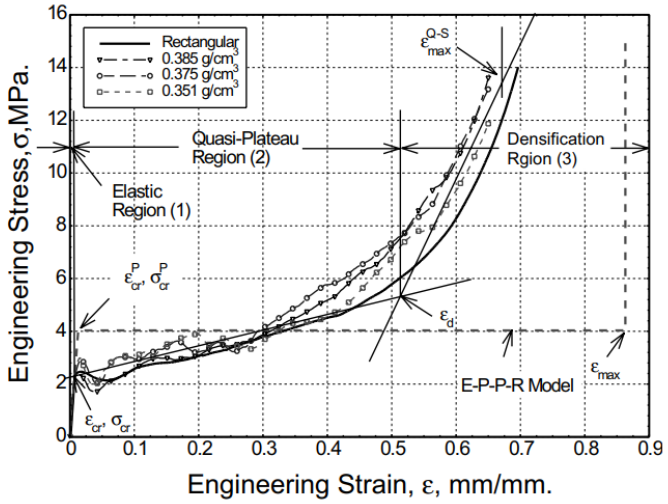

Figure 2.14 - Quasi-static compression behaviour of metal foams [38].

Tensile testing [42] is a fundamental method for evaluating key mechanical properties, including Young's modulus, Poisson's ratio, ultimate tensile strength, and yield strength. The primary outcome of this test is a direct stress-strain curve, which provides insight into the material's deformation behaviour under tensile loading. Figure 15 presents a representative stress-strain curve for metal foams, highlighting two critical points: the yield strength and ultimate tensile strength, as well as the quasi-elastic initial stiffness, which characterizes the material's response in the early stages of loading.

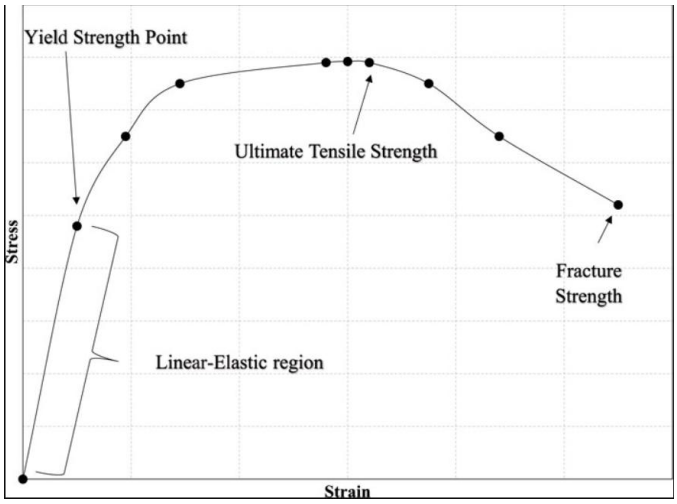

Figure 2.15 - Tensile testing stress-strain curve for metal foams [42].

2.2.5.2 Damping Capability

Metal foams exhibit exceptional damping capabilities far beyond those of their fully dense parent metals, a feature that has attracted considerable attention for passive noise and vibration control in automotive, aerospace, and civil-engineering structures [43]. This enhanced performance stems primarily from hysteresis damping: as a foam undergoes cyclic loading, microscopic sliding and slipping along cell walls and pore interfaces dissipate mechanical energy as heat. Indeed, the internal friction inherent to the foam's cellular network can increase the loss factor by up to an order of magnitude compared to the base metal [36].

Crucially, the damping response of a metal foam is not an intrinsic material constant but rather a function of its specific morphology. Variations in pore size, distribution, cell-wall thickness, wall corrugations, and micro-cracks all influence how effectively the structure dissipates energy, meaning two foams of identical overall density may display markedly different loss factors [44]. Experimental studies on AlSi12 foams illustrate this density dependence: samples at 20 % relative density (approximately 0.5 g/cm^3) exhibit nearly twice the loss factor of their fully dense, powder-metallurgy precursor, even though the dense precursor already surpasses conventional cast aluminium alloys in damping performance. As density increases, the loss factor

decreases yet remains largely independent of excitation frequency and tends to grow with strain amplitude, which is evident in Figure 16 [45].

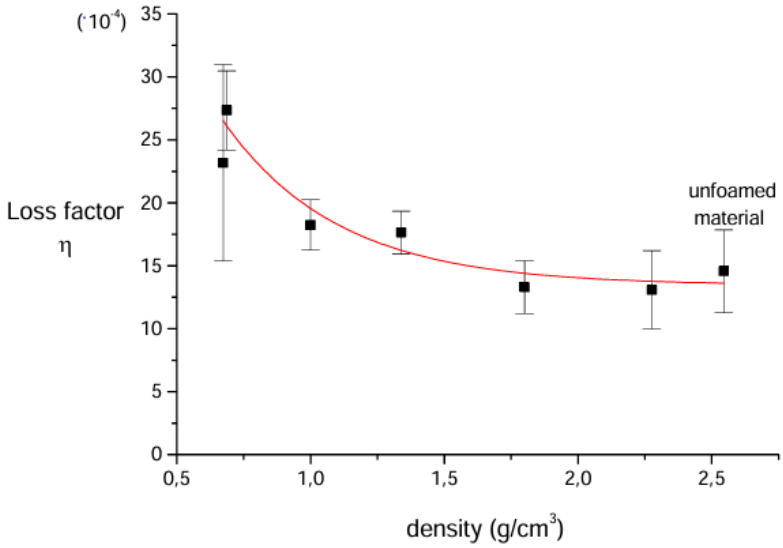

Figure 2.16 - Loss factor of a series of AlSi12 foams measured at 1kHz and room temperature [44].

These characteristics, exceptional hysteresis damping, morphology-sensitive loss behaviour, and demonstrated density-dependent performance, together underscore the multifunctional potential of metal foams. By combining low mass and structural rigidity with superior vibration absorption, foamed metals provide a highly versatile solution for engineering applications where dynamic energy absorption is critical.

2.2.5.3 Sound absorption and vibration suppression

Metallic foams have gained increasing attention as high-performance sound-absorbing materials due to their unique structural and physical characteristics. Materials are typically classified as highly efficient sound absorbers when their average sound absorption coefficient exceeds 0.56 [46]. Metallic foams, in particular, not only meet this criterion but also offer superior mechanical integrity, allowing them to function simultaneously as structural and acoustic materials. This dual functionality, coupled with long service life, recyclability, and environmental sustainability, makes metal foams especially attractive for modern engineering applications [46].

Among various metal foams, aluminium foams stand out for their extensive documentation and adoption in acoustically demanding environments, notably in aerospace and automotive industries [47]. The acoustic absorption capacity of aluminium foams is attributed to their porous structure, especially when the foam features partially open cells. According to Lu et al. [48], sound absorption improves significantly as the pore size decreases, suggesting that pore morphology is a key design parameter for acoustic optimization.

The sound absorption process in metallic foams can be analytically described by the following energy balance equation:

$$E_i = E_r + E_a + E_t \quad (1)$$

Where E_i, E_r, E_a, and E_t are the incident, reflected, absorbed, and transmitted acoustic energy, respectively [49]. Although general acoustic theory recognizes five dissipation mechanisms, in metallic foams, sound energy attenuation is predominantly governed by three: viscous losses, thermal-elastic damping, and resonance effects as depicted in Figure 17 [47]. Viscous dissipation occurs as air is forced in and out of the foam's pores under sound pressure, causing energy loss due to fluid friction. Thermal-elastic damping results from vibrations of air within the foam cavities rubbing against pore walls, transforming mechanical energy into heat. Lastly, resonance-based absorption emerges from Helmholtz-like effects within interconnected pores, especially when pore dimensions align with specific acoustic wavelengths.

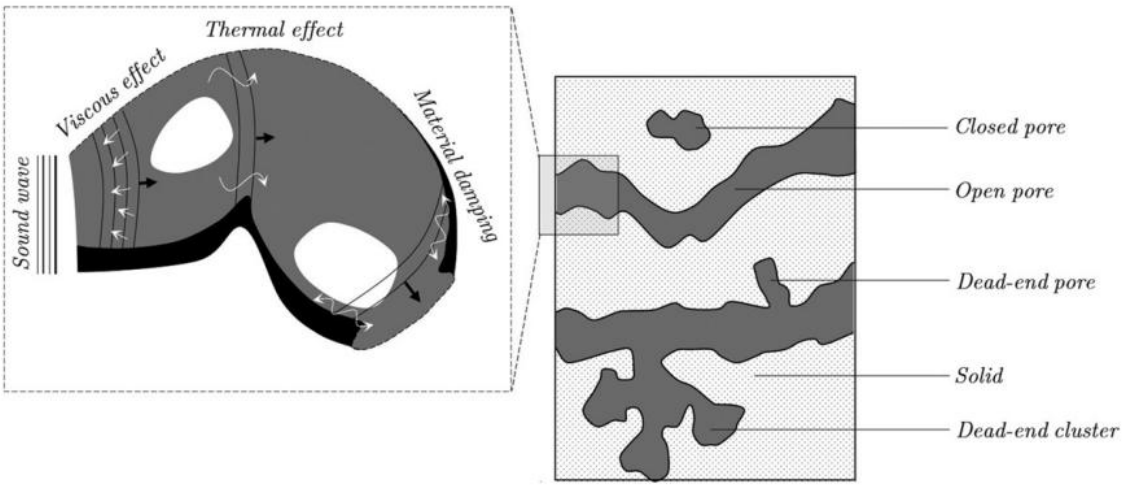

Figure 2.17 - Energy absorption mechanism and pore types in metallic foams [47].

To optimize these effects, a metallic foam must possess a sufficiently interconnected pore network, uniformly distributed across its thickness. This facilitates multiple pathways for sound waves, enhancing the likelihood of energy dissipation through all three mechanisms [47].

Quantitatively, the sound absorption coefficient (α) is a widely used parameter to assess acoustic performance. Defined as the fraction of incident sound energy absorbed by a material, a coefficient of 0.9 indicates that 90% of the sound is absorbed [24].

Further empirical studies have elucidated the influence of foam morphology on sound absorption. For open-cell foams, samples with the smallest pore size demonstrated superior absorption in the presence of an air gap, likely due to the increased surface area enhancing viscous and thermal losses. However, when an air gap was introduced behind the foam, the performance of those with medium pore

sizes was superior, suggesting that a resonance effect similar to Helmholtz absorption becomes dominant in such configurations [50]. Reported performance metrics for these foams include peak absorption coefficients between 0.96 and 0.99, noise reduction coefficients (NRC) ranging from 0.44 to 0.62, and absorption peaks spanning 1500–3500 Hz [51].

Conversely, closed-cell aluminium foams generally exhibit lower intrinsic absorption, attributed to their less permeable structure. However, performance can be drastically enhanced through perforation. Experimental results showed that at identical porosity, foams with larger cell diameters had better sound absorption coefficients. Moreover, perforating the material significantly improved performance, with peak coefficients rising from 0.46 to 0.96 as perforation ratios increased from 0.5% to 2% [51]. These improvements are largely due to the creation of Helmholtz-like resonant cavities, especially effective in the low-frequency range. Increasing cavity thickness was also found to enhance absorption at lower frequencies, albeit at the cost of performance in higher frequency bands [51].

In summary, the acoustic efficiency of metallic foams is intimately tied to their cell structure, porosity, perforation characteristics, and backing configurations. Understanding and manipulating these variables allows engineers to tailor metallic foams for specific acoustic applications, achieving high absorption efficiency across desired frequency ranges.

2.2.5.4 Thermal management and heat transfer

Heat transfer, the movement of thermal energy due to temperature differences [52], occurs by conduction, convection, and radiation [53]. While non-metallic foams act as insulators due to their low thermal conductivity, open-cell metal foams have much higher effective thermal conductivities (often by an order of magnitude) and are therefore used not for insulation but specifically to enhance heat transfer rates [54].

Within a metal foam, heat transfer occurs by a combination of mechanisms: conduction through the interconnected solid metal bands, radiation between solid surfaces, conduction through the fluid in the pores, and convection between the solid and the fluid flowing through the pores [53]. Although all modes can contribute, conduction through the highly conductive solid matrix is often the dominant pathway, while convection becomes critical when a fluid flows through the structure. The structural properties of the foam are key influences. Decreasing porosity (or equivalently increasing relative density) increases the effective thermal conductivity by increasing the volume fraction of conductive solid metal [53]. Experimental studies confirm this trend, showing that the volumetric heat transfer coefficient generally increases with decreasing porosity for a given Reynolds number [55]. It has also been reported that heat transfer performance improves with decreasing cell size [56]. However, optimisation is crucial as studies have indicated the existence of an optimum porosity for overall thermal performance, with one study reporting 80% porosity as optimal under certain conditions [56].

Thermal performance in convective scenarios is typically quantified using an effective heat transfer coefficient H_c, which relates the surface heat flux, q, to the characteristic temperature difference, ΔT [57]:

$$q = H_c \cdot \Delta T \quad (2)$$

A higher H_c signifies more efficient heat removal. The proven ability of metal foams to significantly increase this coefficient explains their use in demanding applications such as compact heat exchangers, electronics cooling, and combustors [54]. For example, the incorporation of copper metal foam into heat exchangers has been shown to increase heat transfer coefficients by up to 2.5 times compared to systems without the foam [58], demonstrating their significant potential for improving thermal management.

2.2.5.5 Electrical properties of metal foams

The electrical conductivity of a metal foam is inherently lower than its parent solid metal because the gas-filled cell interiors are non-conductive. Although one might naively expect conductivity to scale linearly with relative density, experiments consistently show a stronger-than-linear dependence. This arises because increasing porosity not only reduces the metallic volume fraction but also increases the tortuosity of current paths and effectively narrows the load-bearing ligaments more than simple volume-fraction arguments predict. Nevertheless, even with this reduction, metal foams retain sufficient conductivity for effective grounding and electromagnetic shielding applications [24].

In addition to porosity, microstructural defects, such as wall corrugations, incomplete sintering of cell walls, broken ligaments, and micro-cracks, can introduce significant scatter in measured conductivity values. Predictive models must therefore be applied with caution, as idealized equations may overestimate performance in the presence of these imperfections [59]. For open-cell foams produced via the spacer (replication) method, pore size further modulates conductivity: at fixed porosity, smaller pores increase the gas–solid interfacial area, trapping more air and reducing conductivity, whereas larger pores promote stronger metallurgical bonding and higher conductivity. However, excessively large pores can lead to ultra-thin, fracture-prone ligaments that again diminish the conductive network [60]. Anisotropy in conductivity has also been observed when pores are elongated; this anisotropy diminishes at higher porosities, and foams with very high porosity approach quasi-isotropic electrical behaviour [61].

Accurate characterization of foam conductivity commonly employs a four-probe resistivity measurement to mitigate contact resistance effects. Four collinear probes, with spacings s_1, s_2 and s_3, are pressed onto a sufficiently thick sample so that edge effects are negligible. A constant current I is applied through the outer probes (P1 and P4), and the resulting voltage drop V is measured between the inner probes (P2

and P3) as shown in Figure 18. Under the semi-infinite approximation, the foam's bulk resistivity is given by [62]:

$$r = \frac{2\pi\left(\frac{V}{I}\right)}{\left[\frac{1}{s_1} + \frac{1}{s_3} - \frac{1}{s_1 + s_2} - \frac{1}{s_2 + s_3}\right]} \tag{3}$$

The electrical conductivity σ is the reciprocal of ϱ, and the resistance R_f of a foam specimen of length l and cross-sectional area a normal to current flow follows:

$$R_f = r\frac{l}{a} = \frac{l}{\sigma a} \tag{4}$$

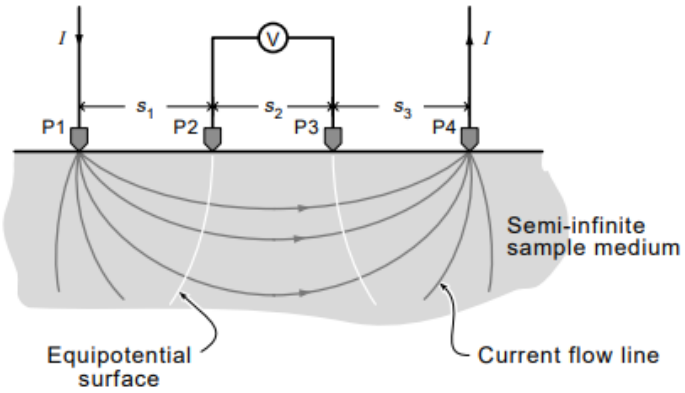

Figure 2.18 - Four-point probe method for measuring the electrical conductivity of metal foam [62].

2.2.6 Applications

Cellular metallic materials are finding an increasing range of applications, as illustrated in Figure 19. Whether a suitable porous metal or metal foam can be found to solve a given problem depends on many conditions, summarised here by the following keywords:

- Morphology: type of porosity needed (open versus closed), amount of required porosity, size scale of porosity desired, total internal surface area of cellular material required;
- Metallurgy: metal or alloy, or microstructural state required;
- Processing: possibilities for shaping the foam or cellular solid or for manufacturing composites between the foam and conventional sheets or profiles;
- Economy: cost issues, suitability for large volume production [6].

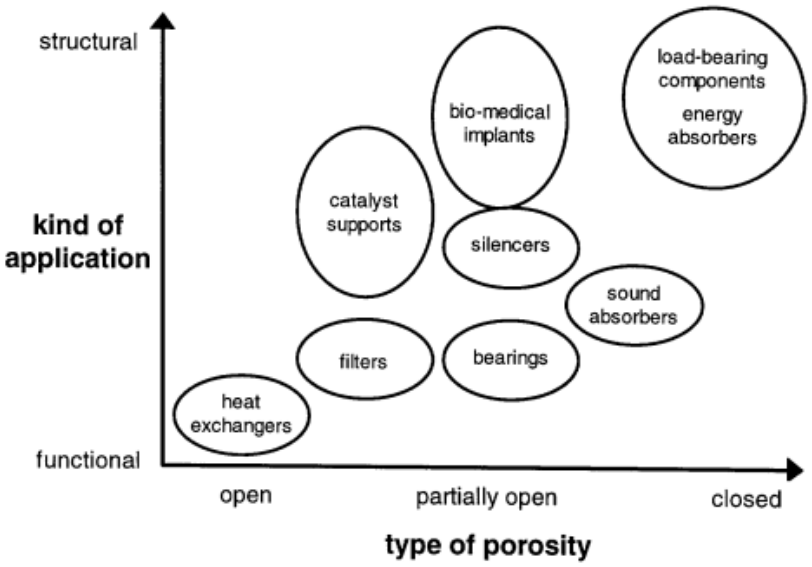

Figure 2.19 - Applications of cellular metals grouped according to the degree of "openness" needed and whether the application is more functional or structural [6].

The existing applications of metal foams are wide-ranging, and new uses are continually emerging [63]. Therefore, metallic foams can be classified according to their applications, as depicted in Figure 20.

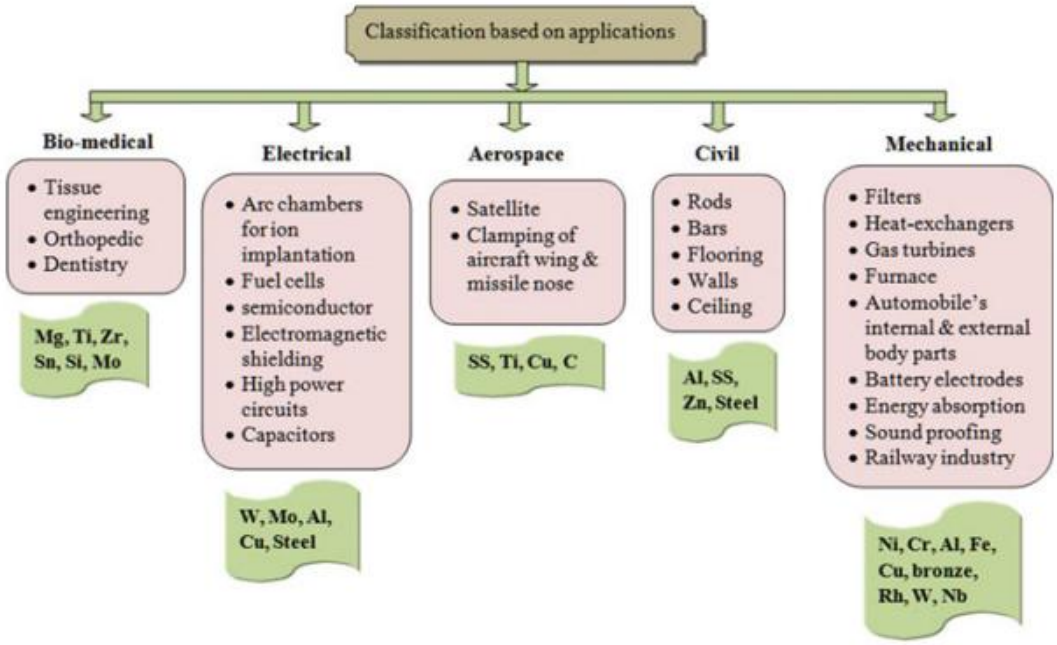

Figure 2.20 - Classification of metal foam materials based on their applications [36].

As the above examples show, aluminium is the most popular material used in metallic foams, though other materials such as titanium, copper, magnesium, and zinc are also used [64].

Metal foams, with their intricate cellular structure and unique material properties, have become essential across various industries, including automotive engineering, aerospace, biomedicine, and architecture. Their combination of low density, high mechanical strength, energy absorption, and thermal conductivity enables their use in demanding applications that require multifunctional and high-performance materials [24][65].

- Impact Absorption: One of the primary applications of metal foams is in energy absorption systems, particularly in industries where safety is paramount, such as automotive and aerospace. Metal foams are incorporated into impact zones to absorb and dissipate energy during collisions, thereby protecting both the structural integrity of the vehicle and the safety of passengers [6][24]. They are commonly used in automotive body panels and structural supports, which benefit from their shock-absorbing capabilities to minimize the effects of impact. An example can be seen in Figure 21.

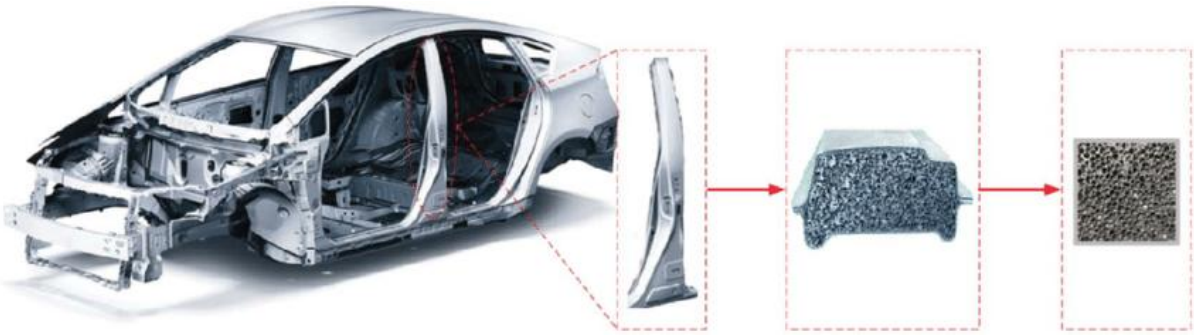

Figure 2.21 - The typical foam-filled tubular thin-walled structure in a vehicle [66].

- Filtration and Catalyst Supports: The porous nature of metal foams makes them highly suitable for filtration and as catalyst supports in chemical and purification processes. Various examples are shown in Figure 22. In air and water filtration systems, they allow effective particle retention while maintaining continuous fluid flow. Additionally, their extensive surface area makes them ideal substrates for catalysts, enhancing chemical reaction efficiency by providing a large reactive surface, which is valuable in both industrial and environmental applications [65].

Figure 2.22 - Different pure metallic and alloyed foam pellets for catalysis in packed bed reactor vessels [67].

- Biomedical Implants and Medical Devices: In the biomedical field, metal foams, especially titanium-based alloys, are increasingly utilized in implants due to their biocompatibility and structural similarity to bone tissue. Figure 23 shows an example of this type of application. Their mechanical properties make them excellent bone substitutes in orthopaedic implants, promoting osseointegration by supporting natural bone tissue growth within the metal structure. This combination of stability and compatibility improves both the durability and comfort of implants for patients [6][65].

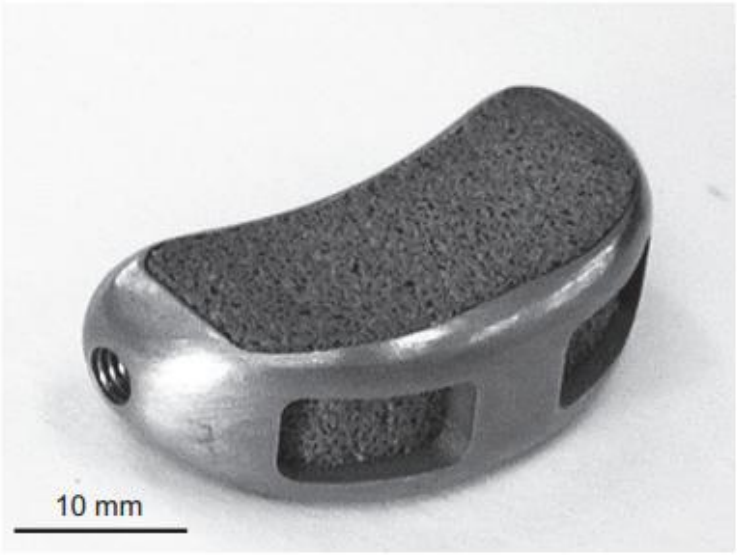

Figure 2.23 - Device of bioactive titanium (Ti) foam for lumbar interbody fusion [68].

- Construction and Architecture: In the construction and architectural sectors, metal foams offer a blend of structural integrity and aesthetic appeal. They are employed in building panels, ceilings, and decorative elements where high

strength-to-weight ratios are beneficial. Their unique appearance and lightweight properties make them ideal for applications where both structural efficiency and visual impact are desired, aligning well with modern energy-efficient and durable architectural designs. Figure 24 shows the ceilings of an audience hall and a restaurant covered by Alusion foam provided by Cymat (Mississauga, ON, Canada) [65].

(a) (b)

Figure 2.24 - Ceiling of (a) audience hall; and (b) restaurant covered by Alusion foam for sound control (Cymat) [65].

- Thermal Management and Heat Dissipation: Metal foams are also widely used in thermal management systems, especially in applications requiring efficient heat dissipation an example is shown in Figure 25. In high-performance electronics and industrial equipment where temperature control is crucial, the porous structure of metal foams increases surface area contact and facilitates thermal exchange, enhancing cooling efficiency and reducing overheating risks [6]. This makes them particularly effective as heat sinks and in other high demand cooling applications.

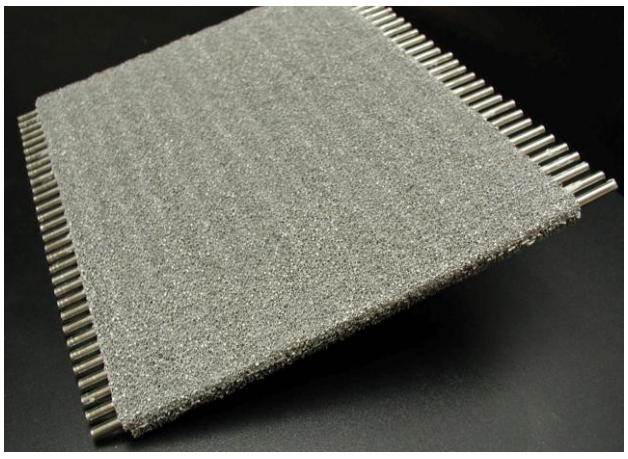

Figure 2.25 - Metal foam compact heat exchanger for high temperature service [64].

The exceptional multifunctionality of metallic foams highlights their potential for applications beyond traditional structural and thermal uses. Their electrical and thermal conductivity, combined with a large specific surface area, make them particularly attractive for electrochemical processes [6-7].

In this context, metallic foams have recently gained attention as advanced electrode materials in environmental technologies, particularly water treatment systems [70-72]. Their open, conductive structure enhances electrochemical activity and facilitates mass transfer while minimising electrode passivation, all of which are critical factors in electrocoagulation systems [70][73-74].

The following section introduces the fundamentals of industrial wastewater treatment and electrocoagulation. It provides a theoretical framework for using metallic foams as high-efficiency electrodes in this process.

2.3 Industrial Wastewater and Electrocoagulation

Water pollution arises when substances that alter the chemical or biological integrity of water are released into natural systems, negatively affecting human health and ecosystems [75]. With increasing urbanization and industrialization, the discharge of domestic and industrial wastes has become one of the major contributors to global water contamination [76].

Industrial activities, in particular, are responsible for a large share of this pollution, as almost all water used in production processes becomes wastewater. These effluents originate from various sectors, such as textiles, food processing, metallurgy, petrochemicals and chemicals, and contain complex mixtures of organic and inorganic substances, heavy metals, oils and dyes [77]. If not treated properly, such discharges can lead to oxygen depletion, eutrophication, and long-term damage to ecosystems.

Among the various treatment methods, electrocoagulation (EC) has emerged as one of the most effective electrochemical processes for treating wastewater, offering high pollutant removal efficiency and environmental sustainability. In the EC process, a low-intensity direct current is applied between metallic electrodes, which are typically made of aluminium or iron and act as sacrificial anodes. The oxidation of these anodes releases metal ions into the solution, while hydrogen gas is simultaneously generated at the cathode [9]. The dissolved metal ions undergo hydrolysis to form metal hydroxide complexes, mainly $Al(OH)_3$ or $Fe(OH)_3$, which can neutralise the surface charge of colloidal particles, organic molecules, and emulsified oils. This charge neutralisation reduces the electrostatic repulsion between particles, facilitating their aggregation into larger flocs that can be separated by sedimentation or flotation. Figure 26 illustrates these interactions [10].

The EC mechanism is closely related to conventional chemical coagulation, whereby charged particles are destabilised by reducing their electrical double layer potential.

However, EC has one major advantage: the coagulant species are generated in situ through the electrolytic dissolution of the anode, rather than being added externally. This eliminates the need for chemical dosing, reduces operational complexity, and significantly minimizes secondary pollution from residual reagents [10].

Furthermore, the hydrogen bubbles formed at the cathode naturally float aggregated flocs to the surface, thereby enhancing the efficiency of solid–liquid separation. Consequently, EC integrates coagulation, flotation, and limited electrooxidation processes within a single reactor. This multi-functionality enables the removal of a broad spectrum of pollutants, including heavy metals, dyes, suspended solids and dissolved organics [9].

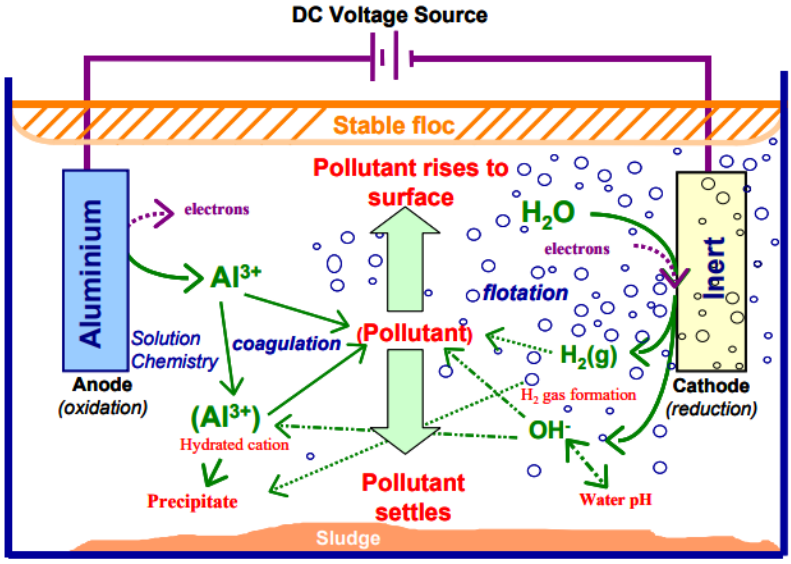

Figure 2.26 - Interactions occurring within an electrocoagulation reactor [11].

2.3.1 Chemical Oxygen Demand

Determining the chemical oxygen demand (COD) is a way of quantifying the efficiency with which pollutants are removed during electrochemical treatment. COD represents the amount of oxygen required to chemically oxidise the organic matter present in a water sample and is one of the most widely used parameters for evaluating wastewater quality. A higher COD value indicates a greater concentration of oxidizable material, which typically correlates with a lower level of dissolved oxygen in the water. Such conditions can have detrimental effects on higher aquatic life forms. The primary objective of wastewater treatment processes is therefore to reduce COD levels, ensuring improved water quality [12].

As in the wider European Union, the discharge of industrial effluents into public sewer networks in Portugal is strictly regulated to ensure compatibility with municipal wastewater treatment plant operations.

According to Article 55 of Regulation No. 448/2024, which sets out the limits for discharging wastewater into public drainage systems, the maximum permissible chemical oxygen demand (COD) is 1,000 mg O_2/L.

This value represents the threshold above which industrial effluents must undergo pre-treatment before being discharged into municipal systems.

In accordance with applicable Portuguese legislation, the final effluent must comply with the discharge conditions set out in Decree-Laws Nos. 236/98 of 1 August and 152/97 of 19 June, as amended. The value of 150 mg O_2/L defines the maximum permissible COD concentration for effluent discharge in order to ensure that treated wastewater does not compromise receiving water bodies or the performance of downstream treatment systems.

2.3.2 Energy Consumption for Electrocoagulation

Energy consumption is one of the most decisive parameters in assessing the technical and economic viability of EC. Although EC is regarded as a sustainable and highly efficient technology for wastewater treatment, its operational costs are strongly influenced by electrical energy requirements [78].

The energy demand mainly depends on current density, conductivity, electrode spacing, and reaction time. Higher conductivity reduces electrical resistance, enabling operation at a lower voltage for a given current and improving energy efficiency [79].

Table 4 shows various energy consumption ranges of EC for different types of wastewaters. The values in the table depend on several factors, such as the intensity of the current, time, the volume of effluent, its conductivity, the material of the electrodes and effluent, and the distance between the electrodes.

Table 2.4 - Reported energy consumption ranges for electrocoagulation.

	Type of Electrode	Energy consumption ($kWh \cdot m^{-3}$)	Reference
Domestic Wastewater	Iron	0.49-0.54	[80]
Municipal Wastewater	Iron	4.5-5	[81]
Munitions Industry Wastewater	Iron	2.55	[82]
Textile Wastewater	Aluminium	0.05-1.30	[83]
Slaughterhouse Wastewater	Mild steel	4.19	[84]

3 MATERIALS AND METHODS

3.1 Process of Open-Cell Aluminium Foams in the Solid State

The present work focuses on the solid-state production of open-cell aluminium foams. This chapter outlines the experimental procedure, covering material preparation, processing parameters, and the foam fabrication methodology.

As detailed in Section 2.2.4, metallic foams are fabricated via solid-state routes by mixing the metallic matrix, aluminium in this case, with a space holder or porosity-inducing agent. This mixture is prepared in a controlled proportion and subsequently consolidated through compaction, extrusion, or other solid-state techniques to form a precursor material. Removal of the space holder then produces the desired porous structure.

In this study, axial compaction was selected as the manufacturing route. Aluminium was mixed with sodium chloride (NaCl), which acted as a space holder, and the mixture was uniaxially compacted into briquette-like precursors. These precursors were then subjected to subsequent processing steps to remove the NaCl, resulting in open-cell aluminium foams with controlled percentage porosity.

The definition of input parameters is of fundamental importance, as they directly influence the morphological and mechanical characteristics of the produced foams. In this study, two primary input variables were considered:

- the type of salt employed as a space-holder;
- the type of aluminium used as base material.

These variables were selected due to their potential to influence the foam's pore morphology, distribution, and mechanical behaviour. Additional parameters, such as compaction force, sintering temperature, and target porosity, were standardized to ensure process reproducibility and reliable comparison between different sample sets.

Based on extensive prior research conducted at the host institution, a compaction force of 400 kN and a sintering temperature of 400 °C were adopted for all experiments [17]. These parameters were identified as optimal for promoting effective particle bonding and dimensional stability, while maintaining the open-pore architecture essential for foam functionality. A target porosity of 60% was also established, as this level provides a well-documented balance between low density and sufficient mechanical strength, influencing critical performance indicators such as stiffness, plateau stress, and energy absorption capacity [17].

By establishing these processing conditions, the experimental plan allows for the systematic investigation of how the aluminium type and space holder material affect the final structure and mechanical performance of the foams.

To assess the effectiveness of the selected processing parameters and to characterize the produced materials, several output parameters were defined and analysed. These include:

- Stress at various deformation levels;
- Relative density;
- Microhardness;
- Degree of deformation and plateau stress;
- Energy absorption capacity.

Together, these parameters provide a comprehensive evaluation of the structural integrity, mechanical behaviour, and overall performance of the fabricated aluminium foams. Establishing correlations between the input and output parameters is expected to contribute to a deeper understanding of the relationships between processing conditions, microstructural evolution, and functional properties, thereby supporting the optimization of solid-state production routes for metallic foams.

3.1.1 Materials

Building on the description of the aluminium foam production method presented in the previous chapter, as well as the definition of the input and output parameters, this chapter focuses on the fundamental materials used in the manufacturing process: the aluminium alloys and the salt types.

3.1.1.1 Type of Aluminium

The base material for metal foam production in this study consisted of aluminium alloys 360, 380, 6082, and 7075, supplied in the form of machining chips. The chemical compositions of these alloys are detailed in Table 5.

The machining chips were obtained through a milling process, where cold compressed air was employed as the cooling medium. This method ensured that the chips remained free from contamination by cooling and lubrication fluids, preserving their chemical purity.

In addition to providing a consistent and controlled raw material for metal foam fabrication, the use of machining chips aligns with sustainable manufacturing practices by recycling aluminium waste from machining processes. By repurposing these chips, this study contributes to reducing material waste and optimizing resource efficiency in metal processing.

To ensure consistency and reproducibility in the experimental process, all chips were produced using the same milling parameters to guarantee a uniform volume and morphology across different alloy types. This standardisation minimises variability, enabling the analysis to focus solely on the intrinsic material properties and their

impact on foam structure and mechanical performance. Table 6 follows Table 5 and contains all the different properties of the chosen alloys.

Table 3.1 - Chemical composition of the aluminium alloys used for chips obtaining (values in %) [85,86,87].

	Al	Si	Mg	Cu	Zn	Fe	Mn	Ni	Ti
Al 360	87.0 – 91.0	9.0 – 10.5	0.4 – 0.6	≤ 0.60	≤ 0.50	≤ 1.30	≤ 0.35	–	≤ 0.15
Al 380	78.0 – 84.0	7.5 – 9.5	≤ 0.10	3.0 – 4.0	≤ 3.00	≤ 1.30	≤ 0.50	≤ 0.50	≤ 0.20
Al 6082	95.2 – 98.3	0.7 – 1.3	0.6 – 1.2	≤ 0.10	≤ 0.20	≤ 0.50	0.4 – 1.0	–	≤ 0.10
Al 7075	87.1 – 91.4	≤ 0.40	2.1 – 2.9	1.2 – 2.0	5.1 – 6.1	≤ 0.50	≤ 0.30	–	≤ 0.20

Table 3.2 - Mechanical and Physical Properties of Aluminium Alloys [85,86,87].

	Density (g/cm^3)	Tensile Modulus, E (GPa)	Hardness (HB)	Tensile Strength (MPa)	Yield Strength (MPa)	Electrical Conductivity ($S/m)\times10^7$
Al 360	2.66	71.0	75	317	165	1.22
Al 380	2.76	74.0	80	324	159	1.33
Al 6082	2.70	70.0	105	340	310	2.63
Al 7075	2.81	71.7	150	560	500	2.33

3.1.1.2 Type of Agent used as a Space Holder

Sodium chloride (NaCl) is a space holder that can only be used for producing metallic foams in the solid state. As discussed in Chapter 2.1, various space holders act as foaming agents when exposed to heat, expanding and creating porosity within the metallic matrix (Chapter 2). However, NaCl does not exhibit this behaviour. Instead, it undergoes a phase transition from solid to liquid at 803°C [88], as shown in Table 7, which prevents it from functioning as an expansion agent.

Table 3.3 - Melting points determined using Thermomechanical Analysis (TMA) and Differential Scanning Calorimetry (DSC) [88].

	Temperature (°C)			
	(TMA) (±0.5%)		(DSC) (±1.0%)	
mol% NaCl	Liquidus	Solidus	Liquidus	Solidus
100	803(±4)	803(±4)	802(±8)	802(±8)
75	716(±4)	661(±3)	710(±7)	655(±7)
60	675(±3)			
51	658(±3)	656(±4)	655(±7)	655(±7)
40	665(±3)			
25	702(±4)	666(±3)	696(±7)	660(±7)
0	776(±4)	776(±4)	770(±8)	770(±8)

In this study, table salt (NaCl) and Himalayan salt were used as space holder materials in the production of open-cell metal foams. The average particle size of the Himalayan salt was measured at 5.2 mm, while the table salt exhibited an average particle size of 4.74 mm. Figure 27 provides a visual representation of the different space holders used in the foam manufacturing process.

(a) (b)

Figure 3.1 - Type of space holders: (a) - Himalaya salt, (b) - Table salt.

A constant mass fraction of 60% was maintained for both types of salt throughout all experimental conditions. The exact selection of this mass fraction was based on findings from previous studies conducted at the Faculty of Electrical Engineering, Mechanical Engineering, and Naval Architecture (FESB) [17], which demonstrated that this ratio is optimal for achieving a well-defined porous structure. Given that salt is a water-soluble material, it was expected that the volume fraction of the space holder would directly correspond to the porosity of the resulting metal foam,

provided that the leaching process was carried out effectively. This assumption is critical, as the removal of the space holder is a key step in ensuring the formation of a fully interconnected porous network within the final foam structure.

3.1.2 Production Method of the Open-cell Aluminium foam

3.1.2.1 Preparation and Briquetting of Samples

During the pre-testing phase, eight metal foam briquette samples were prepared, all of which were designed to exhibit the same target porosity level. Each sample was compacted using identical uniaxial compression forces and subjected to the controlled thermal conditions defined in the earlier parameter selection. This procedure was intended to ensure the reproducibility and comparability of the mechanical properties of all the test specimens.

The initial step in the metal foam production process involved the homogeneous mixing of the base material, aluminium alloy chips, with a space holder agent, sodium chloride, which serves to generate the porous structure.

At this stage, due to the fine particle size and low bulk density of the mixture, the resulting material had a high volume-to-mass ratio, making it challenging to handle. Gradual compaction was necessary to reduce its volume and to enable further processing steps.

To carry out this compaction effectively, dedicated tooling had to be developed for both cold and hot briquetting. For the cold compression stage, a custom-fabricated cylindrical steel mould was employed, specifically designed to guarantee uniform compaction. This mould is shown in Figure 28.

Figure 3.2 - Mould used for the preparation of the samples.

A separate tool was required for the hot compaction stage to allow processing at elevated temperatures. Hot compression offers significant benefits when working with metallic chips produced by machining. By reducing the material's flow stress at high temperatures, this method improves the aluminium chips' deformability, making them easier to densify. Additionally, it leads to enhanced homogeneity in the structure of the precursor, which is vital for ensuring the consistent formation of porosity in the final metal foam.

At the onset of this project, the research group already possessed a basic hot extrusion tool. However, in order to adapt the system to the specific demands of this study, modifications were required. The technical drawing outlining the adapted design is shown in Figure 29-(a). Based on this design, the original tool was reengineered to perform both hot compression and direct extrusion under controlled laboratory conditions. The final version of the modified setup is illustrated in Figure 29-(b).

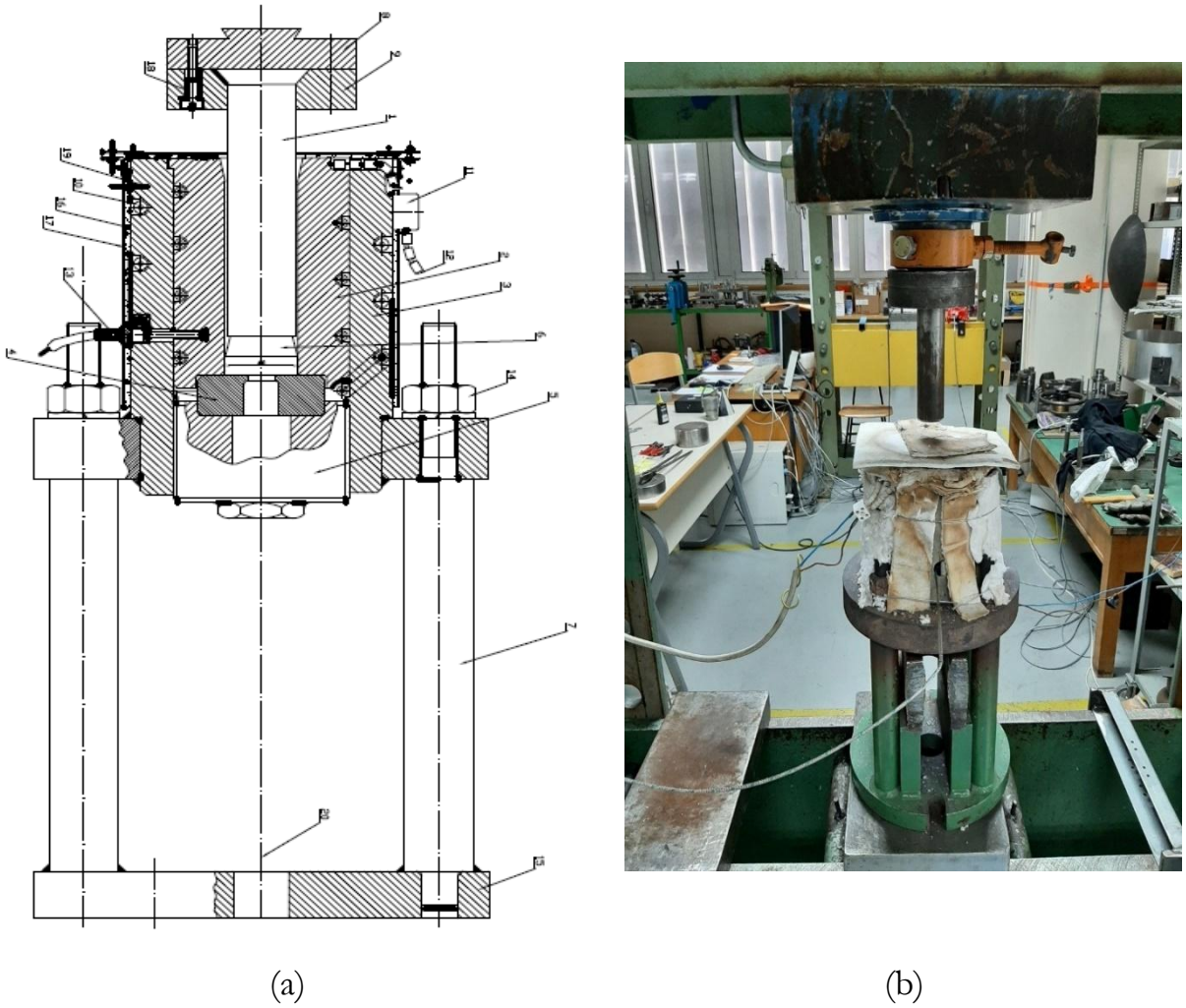

(a) (b)

Figure 3.3 - (a): Design of hot pressing and extrusion tools; (b): Hot pressing and extrusion tool.

Once the briquetting tools were validated and the compaction procedure established, the next step in the process was to determine the exact quantities of aluminium alloy and sodium chloride required for each sample. This mass calculation step was critical to achieve the predefined porosity level and ensure consistency across all specimens, serving as the foundation for the subsequent mixing procedure.

The mass determination process began by first defining the target volume of each individual sample. Based on the geometry of the cylindrical mould and the intended post-compaction height, the sample volume was calculated using the standard volume formula for a cylinder:

$$v_{sample} = v_{NaCl} + v_{Al} <=> \frac{M_{NaCl}}{\rho_{Nacl}} + \frac{M_{Al}}{\rho_{Al}} = \frac{D^2\pi}{4} \cdot h \quad (5)$$

Where:

- v_{sample} is the total volume of sample before briquetting
- v_{NaCl} is the volume of sodium chloride
- v_{Al} is the volume of aluminium alloy particles
- M_{NaCl} is the mass fraction of sodium chloride
- M_{Al} is the mass fraction of aluminum alloy
- ρ_{Nacl} is the density of sodium chloride
- ρ_{Al} is the density of aluminum alloy
- D is the diameter of the hydraulic press recipient
- h is the desired height of sample

Given D=40mm and h=50mm, the volume is calculated as:

$$v_{sample} = \frac{40^2\pi}{4} \cdot 50 \approx 62{,}8\ cm^3 \quad (6)$$

To achieve the desired porosity level, the volume was then divided between the metallic matrix (aluminium alloy chips) and the space holder (sodium chloride). The theoretical densities used for this calculation were 2.70 g/cm³ for aluminium and 2.17 g/cm³ for sodium chloride. Applying the predefined porosity target and assuming complete filling of the mould volume, the mass of each constituent was calculated using the following formulas:

$$M_{NaCl} = v_{sample} \cdot \varphi \cdot \rho_{NaCl} \quad (7)$$

$$M_{Al} = v_{sample} \cdot (1 - \varphi) \cdot \rho_{Al} \quad (8)$$

Where, φ, is the target porosity. Assuming a target porosity of approximately 60% ($\varphi = 0.60$), the following values were obtained:

$$M_{NaCl} = 62.8 \cdot 0.60 \cdot 2{,}17 = 81\ g \quad (9)$$

$$M_{Al} = 62.8 \cdot (1 - 0.60) \cdot 2.7 = 67{,}8\ g \quad (10)$$

These values ensured consistent total volume and porosity across all samples while facilitating repeatable mixing ratios for preparing the precursor materials. This precise control of mass played a critical role in ensuring reproducible experimental results, guaranteeing that the processing variables would primarily influence the foaming behaviour and final properties of the samples under investigation, rather than being influenced by inconsistencies in the initial composition of the materials.

3.1.2.2 Mixing

Following the accurate mass determination of the aluminium alloy chips and sodium chloride particles, the next critical step in the preparation process was the mixing of the two constituents. This step is fundamental to ensure the homogeneity of the precursor material, as the uniform distribution of the space holder (NaCl) within the metallic matrix directly affects the pore morphology, connectivity, and ultimately the mechanical performance of the final aluminium foam.

To this end, the pre-weighed quantities of aluminium chips and sodium chloride granules were introduced into a clean, dry, sealable glass container Figure 30 (a). The container was then manually agitated and rotated in multiple directions for a period of approximately two minutes. This dynamic and multidirectional motion was essential to promote effective intermixing of the two phases and prevent segregation Figure 30 (b). The mixing duration and technique were established based on preliminary trials, which indicated that a two-minute agitation was sufficient to achieve a visually homogeneous distribution of the space holder within the aluminium matrix.

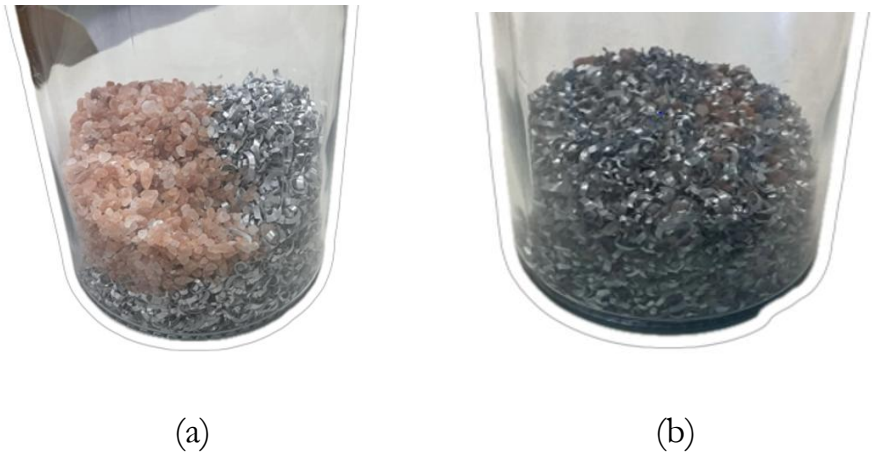

(a) (b)

Figure 3.4 - Mixture of the salt and aluminium alloy: (a)- Before mixing; (b)- After mixing.

3.1.2.3 Cold and Hot Compression

The compaction process plays a fundamental role in the preparation of aluminium foam precursors. The first stage, cold compaction, was carried out by applying a uniaxial load of 400 kN to each sample using a custom-made cylindrical steel mould, as detailed in Chapter 3.1 This process resulted in briquettes with consistent geometry, dimensions, and mass across all specimens, as shown in Figure 31. This phase effectively reduced the volume of the chip and space holder mixture, eliminating major voids and ensuring initial consolidation of the precursor structure.

Figure 3.5 - Example of two samples after the cold compression.

Following cold compaction, the second stage, hot compression, was implemented further to enhance the internal cohesion and density of the briquettes. In this context, hot compaction was conducted at a controlled temperature of 400 °C, as outlined in Chapter 3.1. To ensure uniform thermal conditions, the cold-compacted briquettes were preheated. They were placed in a laboratory oven, Figure 32, and maintained at 400 °C for 20 minutes to allow thermal equilibrium throughout the entire volume. Simultaneously, the steel recipient was brought to the same temperature using integrated resistance heaters regulated by a PID control system, along with two external, non-regulated heaters to maintain temperature stability.

Figure 3.6 - Sample heating in the oven.

After the preheating stage, the hot briquettes were promptly removed from the oven and placed into the preheated mould. Immediate placement into the heated tool was essential to avoid thermal loss and to preserve the desired processing conditions. The samples were then subjected to a uniaxial compressive load of 400 kN using the hydraulic press, applying the same force as in the cold compaction stage. Upon completion of the pressing operation, the samples were carefully extracted from the die and allowed to cool to room temperature under ambient conditions (Figure 33).

Figure 3.7 - Samples after the hot compression.

3.1.2.4 Sample Cleaning and Cutting

Before any foam characterization can be performed, the sodium chloride space-holder must be completely removed from the briquettes to reveal the open-cell structure. In previous investigations at the host institution, a 60 °C ultrasonic bath (ASonic model) was tried for 30 minutes; however, this method removed only about 20 % of the total salt, as the high-pressure compaction had

caused the aluminium to envelop the central NaCl particles [17]. Consequently, ultrasonic cleaning was not adopted in the current work.

In the present study, all briquettes were cleaned by immersing them in boiling water (100 °C) for 30 minutes. This approach was highly effective, as it leached nearly all of the sodium chloride from the precursor, leaving clean, self-supporting metal foam structures that were suitable for subsequent testing.

Based on these results, boiling water immersion was adopted for all subsequent samples. This method reliably removes the space holder without damaging the aluminium framework, and it only requires common laboratory equipment. This makes the process both efficient and cost-effective. The process is illustrated in Figures 34 (a) and 34 (b).

(a) (b)

Figure 3.8 - Boiling water process: (a)- Boiling the sample; (b)- After boiling.

The sintering step, conventionally used to bond metal particles by heating precursors near the base material's liquidus temperature (method used in chapter 2.2.4.1), was intentionally omitted in this work. In a preliminary study, six briquette samples were produced under identical compaction conditions; three underwent sintering and three did not. Kitchen salt, Himalayan salt, and urea were used as space holders. Microhardness tests revealed that unsintered foams consistently exhibited higher hardness than their sintered counterparts, regardless of the type of solvent used. This is attributed to two factors:

- Cold compaction induces work hardening through dislocation buildup and grain fragmentation;
- Recrystallisation during sintering reduces dislocation density and softens the microstructure.

Density measurements showed no significant difference between kitchen salt and Himalayan salt foams, while urea-based foams, having the smallest space-holder particles, yielded the lowest overall density and the finest pore structure. Energy

absorption tests further demonstrated that sintering substantially improves compressive strength and energy absorption only in urea-templated foams; for kitchen salt and Himalayan salt samples, sintering either had no beneficial effect or degraded performance due to thinner cell walls and inhibited interparticle bonding (oxide layers become more detrimental during high-temperature exposure) [17].

Overall, the highest ratios of compressive strength–to–relative density and energy absorption–to–relative density were achieved by the sintered urea-based foams, confirming that when very fine space-holder particles are used, a brief sintering cycle can be justified. However, Himalayan salt foams achieved comparable performance in the unsintered state, making them a cost-effective alternative that avoids the time, energy, and potential microstructural softening associated with sintering [17]. Consequently, and in accordance with these findings, no sintering was performed in the present study. Cold and hot compaction alone provided sufficient bonding and mechanical integrity for further analysis. After boiling water cleaning and prior to any mechanical testing, each foam briquette was sectioned to improve residual salt extraction and ensure the test specimens were representative. A precision aluminium profile saw was used to cut each sample into rectangular prisms measuring 30 mm in height, 20 mm in width and 20 mm in length. This sectioning step was implemented specifically to expose internal surfaces, facilitating the removal of entrapped NaCl and yielding more authentic, homogeneous foam specimens for subsequent structural and mechanical evaluation, as shown in Figure 35.

(a) (b)

Figure 3.9 - (a): Sample after the cut; (b): Sample after boiling in water again.

3.1.3 Preliminary Assessment of Sample Integrity

After sectioning, all eight foam briquettes were cut into 30 × 20 × 20 mm prisms. Their structural stability was evaluated visually and by simple handling. All specimens withstood the cutting process and exhibited sufficient integrity for further testing except Samples 7 and 8, which fractured completely upon sectioning and were

therefore excluded from subsequent characterization. The following Table shows the sample identification.

Table 3.4 - Sample identification and composition

	Aluminium Alloy	**Space-Holder**	**Al Mass (g)**	**NaCl Mass (g)**	**Porosity (%)**
Sample 1	Al 360	Table Salt	67.8	81.0	60
Sample 2	Al 360	Himalayan	67.8	81.0	60
Sample 3	Al 380	Table Salt	67.8	81.0	60
Sample 4	Al 380	Himalayan	67.8	81.0	60
Sample 5	Al 7075	Table Salt	67.8	81.0	60
Sample 6	Al 7075	Himalayan	67.8	81.0	60
Sample 7	Al 6082	Table Salt	67.8	81.0	60
Sample 8	Al 6082	Himalayan	67.8	81.0	60

In Figures 36 and 37, the post-sectioning conditions of the specimens are shown. Figure 36 illustrates the intact configuration of Samples 1 through 6, confirming their readiness for mechanical and structural testing. Figures 37 (a) and 37 (b) capture the complete failure of Samples 7 and 8 upon cutting, necessitating their exclusion from all subsequent analyses. These remaining six specimens, having demonstrated both dimensional fidelity and sufficient mechanical integrity, were advanced to the density calculation, microhardness and cold compression test phases.

Figure 3.10 - Samples 1 through 6.

The complete fragmentation of samples 7 and 8 during the cutting process can be attributed to a combination of material behaviour and microstructural factors. Al 6082 has a chemical composition and temper that confer relatively high strength, but reduced ductility compared to alloys such as Al 360, Al A380, or Al 7075. During the initial cold and hot compaction stages, the repeated plastic deformation work-hardened the Al 6082 chips more severely, thereby decreasing their ability to accommodate further mechanical strain. When subjected to the shear and bending

stresses inherent in the sawing process, these highly work-hardened regions could not yield plastically, resulting in brittle-like fracture of the briquettes. The Al 6082 briquettes may also have trapped more sodium chloride within their interiors. During hot compaction, the softened aluminium flow can more fully envelop the salt particles. If insufficient salt was removed during cleaning, particularly in deeper, less accessible areas, these internal inclusions act as stress concentrators. Under the localized stress of the cutting blade, microcracks nucleate at the aluminium–salt interfaces and rapidly coalesce, causing complete fragmentation of the sample shown in Figure 37. For all of these reasons, Samples 7 and 8 were excluded from the results and discussion.

(a) (b)

Figure 3.11 – Fragmentation of the excluded samples: (a)- Sample 7 after cutting; (b)- Sample 8 after cutting.

In order to complement the preliminary assessment of sample integrity, the mass and density of each specimen were determined prior to mechanical testing. These parameters provide important baseline information on material consistency and are critical for the subsequent normalization of mechanical properties. The geometric volume (V) of each prism-shaped sample was calculated from its measured dimensions according to:

$$Volume = h \times w \times l \tag{11}$$

Where:

- h is the sample height [mm];
- w the width [mm];
- l the length [mm].

The apparent density (ρ) was then obtained as:

$$\rho = \frac{M}{v} \tag{12}$$

Where:

- M is the mass of the sample [g];
- v its calculated volume [cm³].

The values of the density are presented in the results section.

3.1.4 Microhardness Procedure

In order to assess the local mechanical resistance of the foam cell walls, microhardness measurements were performed on the specimens that maintained structural integrity after preparation. The cross-section of each sample was carefully prepared by hand-sanding with 600-grit silicon carbide paper to produce a smooth, flat surface, which is essential for reliable indentation without altering the microstructure. Indentations were made using a Shimadzu HMV-2T microhardness tester (Figure 38), applying a controlled load to the polished surface.

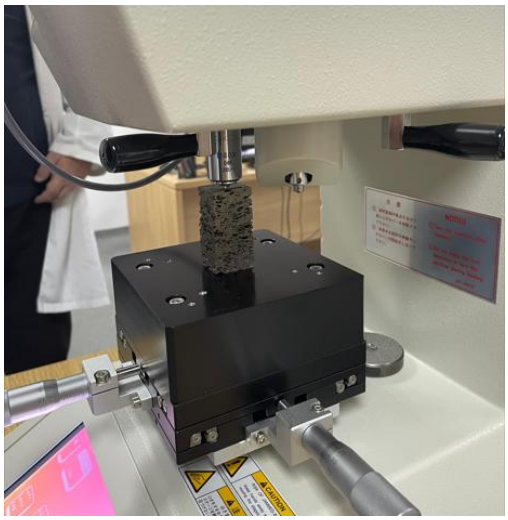

Figure 3.12 - Microhardness Test.

Three separate indentations were placed in distinct regions of each valid specimen to capture the inherent variability of the foam architecture. The resulting Vickers hardness numbers (HV) were averaged to represent the microhardness of each sample.

3.1.5 Cold Compression procedure

The final stage in characterising the prepared aluminium foam specimens was uniaxial compressive testing, which was performed to evaluate their energy absorption capacity. The tests were conducted on a hydraulic press (Figure 39), under displacement-controlled conditions. Each sample was compacted to a final

height of 22 mm, a value selected to ensure comparable levels of deformation across specimens.

Figure 3.13 - Hydraulic press.

To enable accurate monitoring of the applied load and the displacement of the punch during compression, a dedicated measuring device was mounted onto the press. This system incorporated force and displacement sensors, both of which were connected to a data acquisition unit that enabled the real-time measurement of evolving parameters.

During testing, the maximum compressive load recorded was 202,053 N, corresponding to the final stage of deformation when the resistance of the material reached its peak. Figure 40 illustrates this process for one of the samples.

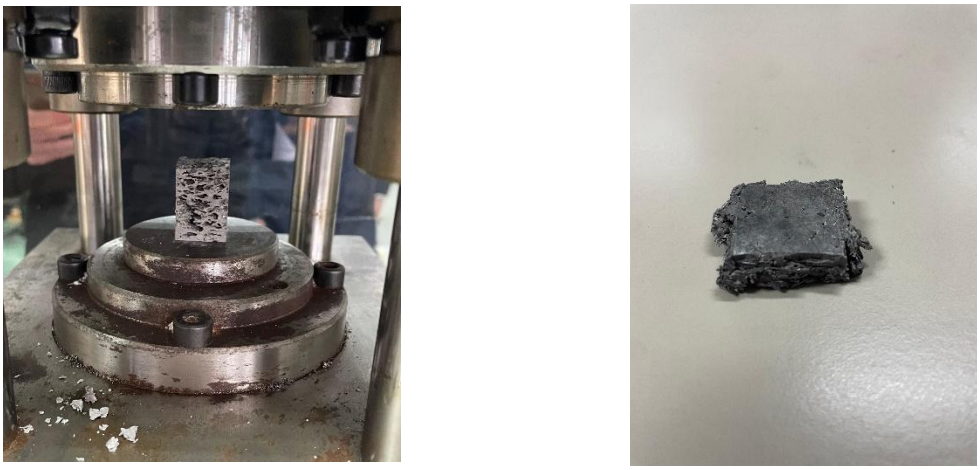

(a) (b)

Figure 3.14 - (a): Aluminium foam before hydraulic press; (b): Aluminium foam after hydraulic press.

A key parameter in the analysis of the compression process is the degree of deformation, defined as:

$$\varphi = ln\frac{h_0}{h} \tag{13}$$

Where:

- φ is the degree of deformation;
- h_0 is the initial specimen height [mm];
- h is the instantaneous specimen height after deformation [mm].

Based on the force and displacement values recorded during the experiments, the true stress (σ) was determined throughout the entire compression sequence according to:

$$\sigma = \frac{F}{a} \tag{14}$$

Where:

- σ is the true strain;
- F is the applied force [N];
- a is the true (instantaneous) cross-sectional area [mm²].

The cross-sectional area was calculated under the assumption of volume conservation, resulting in:

$$a = \frac{a_0 * h_0}{h} \tag{15}$$

$$a_0 = w * L \tag{16}$$

Where:

- w and L represent the initial width and length of the specimen, respectively.

This formulation accounts for the continuous increase of the load-bearing area as the sample shortens during compaction, ensuring accuracy in the determination of stress values.

Data processing was carried out using Microsoft Excel. First, force–displacement curves were plotted from the raw measurements, which were then converted into stress–strain curves using the equations above. These curves formed the basis for subsequent analyses, including the determination of plateau stress, deformation behaviour, and the energy absorption capacity of the foams.

The values of the energy absorbed by the foams were obtained using the following formula:

$$W = \int_0^{\varepsilon^D} \sigma \, d\varepsilon \tag{17}$$

Where:

- W – is the energy absorbed [KJ/m³];
- σ – is the stress [MPa];
- ε – is the strain;
- ε^D – is the densification strain, corresponding to the onset of the densification region in the stress–strain curve.

It is important to note that Sample 3 was excluded from the compression test. Before the experiment, a fragment detached from the upper edge of the specimen during handling, as illustrated in Figure 41. This failure was attributed to the excessive porosity of the cut region, which severely compromised the specimen's structural stability. Due to its lack of mechanical integrity, further testing of Sample 3 would not have produced credible results, so the specimen was discontinued at this stage.

The compression process was successfully repeated for all the remaining specimens.

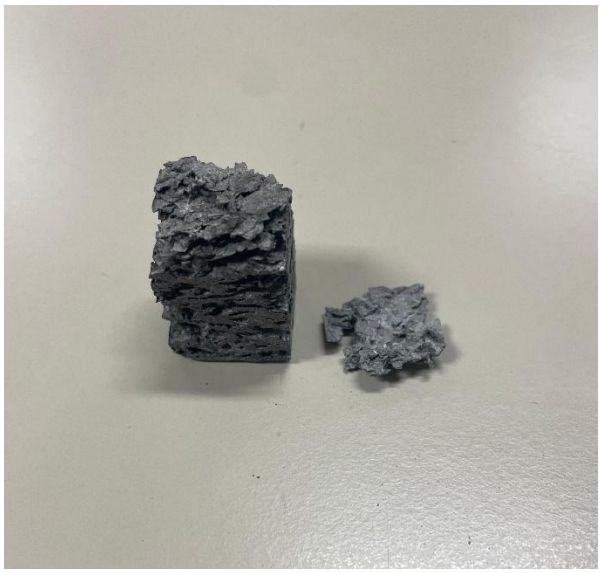

Figure 3.15 - Sample 3 showing localized fracture and loss of material.

3.2 Application of Open-cell Aluminium Foam in Wastewater Treatment

This section outlines the experimental procedure designed to evaluate the performance of open-cell aluminium foams in wastewater treatment. For this purpose, an electrochemical process was employed, which will be described in detail. All experimental steps will be presented systematically, leading to the final results.

To accurately assess the efficiency and behaviour of the aluminium foam during wastewater treatment, a set of critical input and output parameters was defined. The initial parameters measured included:

- Mass of the foam samples,
- Electrical conductivity and pH of the wastewater,
- Initial current intensity, and
- Applied voltage.

Following the electrochemical treatment, the corresponding final parameters were recorded:

- Final mass of the foam (to determine any material loss or corrosion),
- Final conductivity and final pH of the wastewater,
- Final voltage.

These measurements enabled the energy consumption associated with the electrochemical treatment to be calculated, as they provided the necessary electrical parameters recorded throughout the process. However, the evaluation of wastewater purification efficiency and the calculation of the corresponding COD removal rate were carried out separately, based on the absorbance values obtained from the photometric analysis of the effluent samples.

All operating conditions, namely the volume of treated effluent, treatment duration, initial applied current, preparation of wastewater and electrodes, full COD analytical procedure, and equations used to calculate reported quantities, were defined and implemented in accordance with the methodology established by Vicetto [89], in a bachelor's degree internship report conducted at the ISEC.

3.2.1 Material

As the previous foam samples were destroyed during cold compression testing, four new samples were fabricated with the same methods and used twice in the experiments. These were produced using A360 and A380 aluminium alloys, both with an identical porosity of 60%. The samples were cut to dimensions of 26 × 37 mm, a choice that will be justified in subsequent chapters. As in previous samples of

Chapter 3.1, the difference lay in the type of space holder used: standard salt or Himalayan salt. The specific sample configurations are summarized in Table 9.

Table 3.5 - Sample identification.

	Aluminium Alloy	**Space-Holder**	**Al Mass (g)**	**NaCl Mass (g)**	**Porosity (%)**
Sample 1	Al 360	Table Salt	67.8	81.0	60
Sample 2	Al 380	Table Salt	67.8	81.0	60
Sample 3	Al 360	Himalayan Salt	67.8	81.0	60
Sample 4	Al 380	Himalayan Salt	67.8	81.0	60

3.2.2 Electrochemical Process

3.2.2.1 Preparation of the effluent

The first step in the experimental procedure involved preparing the effluent to be treated. For this purpose, wastewater originating from a cork industry was selected due to its representative characteristics and pollutant load. A volume of 450 mL of the effluent was then acidified using sulfuric acid (H_2SO_4) until a pH of approximately 3.0 was reached. This adjustment was performed to create acidic conditions favourable for electrocoagulation processes. To ensure proper homogenization of the acidic solution, a magnetic stirring plate operating at 230 rpm was used throughout the pH adjustment phase, illustrated in Figure 42.

Figure 3.16 - Preparation of the effluent.

Because of pH reduction, the electrical conductivity of the solution was simultaneously altered. Both pH and conductivity were measured using a benchtop pH and conductivity meter, ensuring accurate characterization of the initial conditions.

3.2.2.2 Preparation of the System and Electrodes

Before the start of the electrochemical treatment, the aluminium foam samples were weighed using an analytical balance to determine their initial mass. This step was essential to quantify any potential mass loss resulting from anodic dissolution during the experiment.

For each experiment, aluminium foam was employed as the anode while stainless steel served as the cathode. To maintain a constant inter-electrode spacing of 10 mm, an acrylic parallelepiped coated with Teflon was used as the supporting structure. All components were insulated with Teflon, apart from the active electrode surface intended for contact with the effluent. The exposed area was fixed at 26 × 37 mm, ensuring consistent experimental conditions across all tests. The complete setup is illustrated in Figure 43.

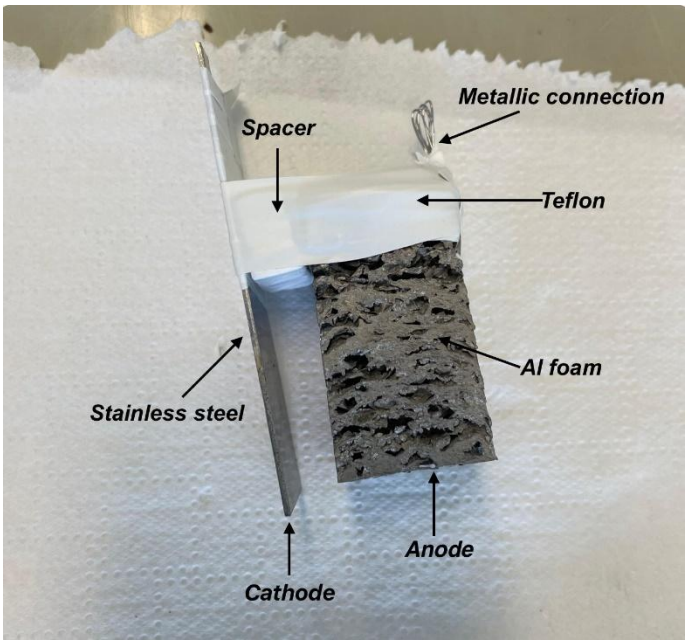

Figure 3.17 - Electrodes Step-up.

3.2.2.3 Electrochemical Reactor

The electrochemical reactor was powered by a direct current (DC) source operating at 0.25 A, a value maintained constant throughout all experiments. Each run was conducted for a total duration of 30 minutes, during which effluent samples were systematically collected for subsequent analysis. To ensure homogeneous mixing and enhance mass transfer between the electrodes and the effluent, a magnetic stirring plate operating at 300 rpm was employed continuously throughout all experiments. The complete configuration of the system can be observed in Figure 44.

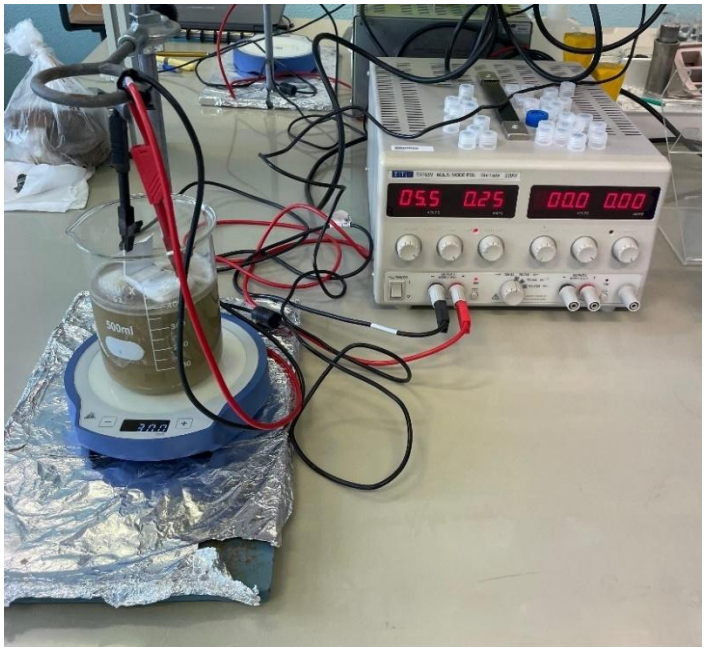

Figure 3.18 - Electrochemical Reactor.

The sampling process was carried out in accordance with a stringent protocol:

- Sample 0 (T_0): collected before the start of each experiment (50 mL).
- Sample 1 (T_1): collected after 1 minute (10 mL).
- Sample 2 (T_5): collected after 5 minutes (10 mL).
- Sample 3 (T_{10}): collected after 10 minutes (10 mL).
- Sample 4 (T_{20}): collected after 20 minutes (10 mL).
- Sample 5 (T_{30}): collected at the end of the process, after 30 minutes (100 mL).

3.2.3 Experimental Procedure of COD analysis

For the COD analysis, the procedure involved the sequential addition of the following reagents to each vial:

1. Digestion solution containing potassium dichromate ($K_2Cr_2O_7$), of which 0.75 mL was added to each vial.
2. Acidic solution consisting mainly of concentrated sulfuric acid (H_2SO_4), of which 1.75 mL was added after.
3. At the end, 1.25 mL of the wastewater sample was added.

Although the digestion and acidic solutions contained additional components (e.g., catalysts), potassium dichromate and sulfuric acid were the primary reagents driving the oxidation process.

Due to the variability in pollutant concentration, some samples needed to be diluted with distilled water before digestion. This adjustment was necessary to ensure that the photometer's absorbance readings would remain within its linear range and to avoid signal saturation. Dilutions were systematically applied at T_0, T_1, T_5, and T_{10}, while for T_{20} and T_{30}, whenever necessary.

To ensure reproducibility and reliability of results, duplicate analyses were performed for each sample at every time interval. In addition, two control samples of distilled water were included in every experimental run to serve as blanks for calibration and baseline correction.

Following reagent addition (steps 1 to 3), all prepared samples were homogenized using a vortex mixer. For each experiment, a total of 14 test tubes were processed (12 wastewater samples corresponding to six time intervals, each in duplicate, plus 2 distilled water blanks). The tubes were then placed in a thermostatic reactor at 150 °C for 2 hours to ensure complete digestion. After digestion, the tubes were allowed to cool gradually, staying inside until 80 °C and then further down to room temperature (≈25 °C). The final analytical step consisted of transferring the cooled samples to the photometer, where absorbance (Abs) was measured at a wavelength of 600 nm, and each one was measured three times. Representative stages of this procedure are shown in Figures 45 (a) and 45 (b).

(a) (b)

Figure 3.19 - (a): Mixing the digestive solution; (b): Reading the solution absorbance.

From these measurements, the Chemical Oxygen Demand (COD) values corresponding to each experimental run were determined. The absorbance readings obtained from the photometer, once corrected with the appropriate blanks, provided the basis for an accurate quantification of COD concentrations at all sampling intervals.

The first step in processing the photometric data consisted of correcting the absorbance values obtained for each sample. This correction was carried out by subtracting the mean absorbance of the blank controls from the raw absorbance of the effluent samples, according to Equation (12):

$$Abs_{final} = Abs_{sample} - Abs_{blank} \quad (18)$$

Where the:

- Abs_{final} represents the correct absorbance,
- Abs_{sample} is the measured absorbance of the effluent sample,
- Abs_{blank} corresponds to the average absorbance of the distilled water blanks.

The corrected absorbance values were subsequently converted into Chemical Oxygen Demand (COD) concentrations by applying the calibration curve established during method validation. The linear relationship obtained is expressed in Equation (13):

$$COD = 0.000330016 \times Abs_{final} + 0.00974307 \quad (19)$$

Where:

- COD is the chemical oxygen demand concentration (mg/L),
- Abs_{final} is the corrected absorbance.

In cases where the effluent samples were diluted prior to analysis, the calculated COD concentrations were multiplied by the respective dilution factor (df), as shown in Equation (14):

$$COD_{final} = COD \times df \quad (20)$$

Where:

- COD_{final} is the final chemical oxygen demand concentration expressed in mg/L,
- df is the dilution factor applied to the sample.

Finally, the efficiency of the treatment was expressed as the percentage reduction in COD relative to the initial concentration measured at T_0. The removal efficiency was calculated using Equation (15):

$$Removal\% = \frac{COD_i - COD_f}{COD_i} \times 100 \quad (21)$$

Where:

- COD_i is the initial COD concentration at T_0 (mg/L),
- COD_f is the COD concentration at a given sampling time (mg/L). This parameter provides a direct measure of the electrochemical process's performance in reducing the organic load of the effluent.

To ensure the robustness and credibility of the COD results, the reliability of the measurements was examined further through a statistical consistency check. For each sampling interval, the standard deviation (SD) of the replicate absorbance measurements was calculated to enable an assessment of the analytical procedure's internal precision. Any value that deviated markedly from the corresponding replicate set, by more than approximately 5% from the mean, was treated as an outlier and excluded from the analysis, reducing the impact of occasional anomalies and strengthening the overall reliability of the reported COD concentrations and resulting pollutant-removal efficiencies.

In addition to pollutant removal efficiency, the energy demand of the electrochemical process was also evaluated, as this parameter is critical for assessing the sustainability and practical applicability of the treatment. The specific energy consumption was calculated according to Equation (16):

$$E_c = \frac{I}{V} \sum_{i=0}^{N-1} \frac{U_i + U_{i+1}}{2} \times (t_{i+1} - t_i) \tag{22}$$

Where:

- E_c is the energy consumption (kWh/m^3),
- I is the applied current intensity (A),
- V is the treated effluent volume (m^3),
- U is the recorded voltage at the power supply (V),
- t is the reaction time (h).

4 RESULTS AND DISCUSSION

This chapter presents and discusses the experimental results obtained in this study. Section 4.1 addresses the mechanical and structural characterisation of the recycled open-cell aluminium foams, including their density, microhardness, and compressive behaviour. Section 4.2 examines their performance as electrodes in electrocoagulation processes, with a focus on pH evolution, conductivity, voltage, COD removal efficiency, and energy consumption. The methodologies used to derive the reported quantities are described in Chapter 3 and are not repeated here.

4.1 Results and Characterisation of the Open-Cell Foams and Discussion.

4.1.1 Density

The measured masses and corresponding apparent densities of the foam specimens are summarised in Figures 46 (a) and (b).

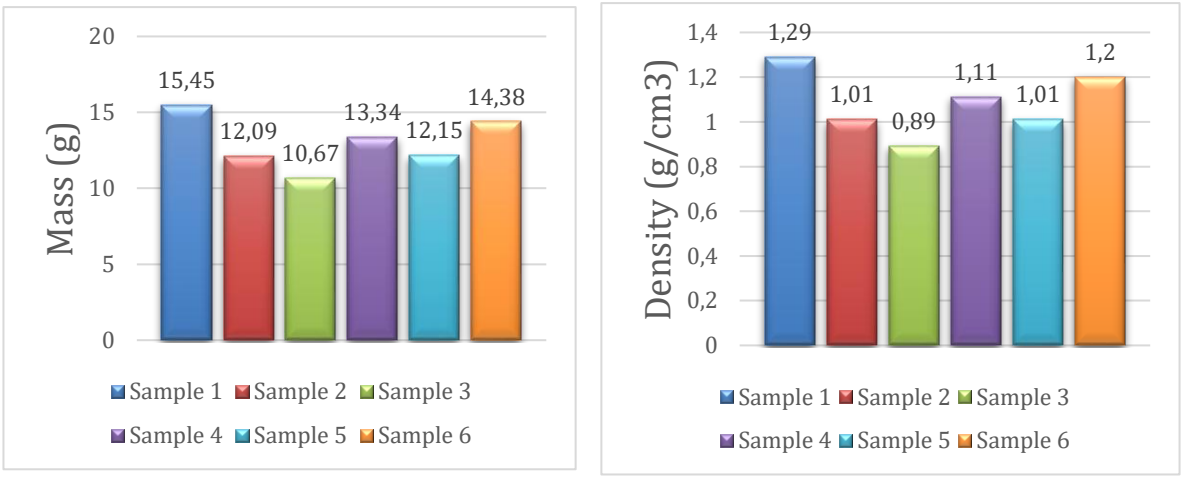

(a) (b)

Figure 4.1 – The measured mass and density of the samples: (a) - Mass results; (b) – Density results.

As expected, all samples of salt-replicated aluminium foam exhibit a substantial reduction in density compared to the theoretical density of solid aluminium alloys (approximately 2.70 g/cm³), which confirms the successful formation of an interconnected porous structure.

The obtained densities range from 0.89 to 1.29 g/cm³. Sample 1 (Al360 – Table Salt) has the highest density (1.29 g/cm³) of all the specimens, while Sample 3 (Al380 – Table Salt) has the lowest (0.89 g/cm³). The remaining foams display intermediate and relatively consistent densities: 1.01 g/cm³ for Samples 2 and 5; 1.11 g/cm³ for

Sample 4; and 1.20 g/cm³ for Sample 6. These differences reflect natural variations associated with the salt as a space holder reproduction method, whereby the level of pore interconnection and strut thickness are influenced by factors such as particle size distribution, packing uniformity, and the degree of chip compaction.

Despite these variations, all values confirm that the recycled aluminium chips were effectively consolidated during hot pressing, enabling continuous metallic ligaments to form after salt leaching. The reduced density is advantageous for the intended electrocoagulation application as lower-density foams typically have a higher internal surface area and improved permeability. These characteristics are both essential to ensure efficient electrolyte diffusion and enhanced anodic dissolution during treatment.

4.1.2 Microhardness

In the microhardness test, two specimens (Samples 3 and 5) could not be reliably evaluated. Sample 3 exhibited extensive surface exfoliation and poor compaction, causing the material to flake under the indenter. Meanwhile, Sample 5 collapsed locally under the applied load due to excessive fragility. As testing these specimens would not produce representative results, they were excluded from the analysis. Figures 47 (a) and (b) illustrate their surface condition. The remaining results are summarised in Table 10.

(a) (b)

Figure 4.2 - (a): Sample number 3; (b): Sample number 5.

Table 4.1 - Vickers Hardness (HV) Measurements.

	HV 1	**HV 2**	**HV3**	**Average HV**
Sample 1	44.3	44.6	46.3	45.1 ± 0.9
Sample 2	38.3	38.2	40.4	39.0 ± 1.0
Sample 3	Not tested – surface exfoliation prevented valid indentations	-	-	-
Sample 4	49.7	50.3	47.7	49.2 ± 1.1
Sample 5	Not tested – structural fragility yielded inconclusive data	-	-	-
Sample 6	48.3	47.7	48.6	48.2 ± 0.4

The measurable specimens exhibited Vickers hardness values ranging from 38.3 to 49.7 HV. Sample 1 (Al360 – table salt) had the highest average hardness, at 45.1 ± 0.9 HV, while Sample 2 had the lowest measurable value, at 39.0 ± 1.0 HV. Samples 4 and 6 displayed intermediate values of 49.2 ± 1.1 and 48.2 ± 0.4 HV, respectively. While these values are lower than those of the bulk alloys, they are consistent with expectations for open-cell foams, where porosity and local microstructural discontinuities significantly reduce the material's resistance to indentation.

The hardness of metallic foams is inherently variable because each indentation probes a distinct local feature, such as a strut centre, a node or a thin ligament adjacent to a pore. This spatial heterogeneity leads to fluctuations that reflect variations in local density and stiffness. Additionally, the compliance of the pore network influences the apparent hardness: deformation beneath the indenter is redistributed through adjacent voids, reducing the measured value relative to that of the solid parent alloy. Interfacial imperfections arising from incomplete chip bonding also contribute to the reduction in hardness by weakening the continuity of the metallic ligaments.

To mitigate local scatter, three indentations were performed on each specimen and averaged. This approach provided a more reliable assessment of the foam's inherent resistance to plastic deformation.

Despite the intrinsic scatter, the obtained results align well with the expected behaviour of the alloys used. Foams produced from Al380 and Al7075 exhibited moderately higher average hardness values than those made from Al360, which is consistent with their alloying additions and strengthening mechanisms in the bulk state.

4.1.3 Cold Compression

This section presents the results and discussion obtained from the cold compression tests. Table 11 summarises the measured height reduction values (h) and corresponding deformation degrees (φ), as determined from the compression test data. These parameters provide an overview of the total strain achieved by each specimen prior to densification. Sample 3 was excluded from this analysis due to structural irregularities, as described in Section 3.1.5, which prevented the acquisition of reliable compression data.

Table 4.2 - Height reduction values (h) and corresponding deformation degrees (φ).

	h_0(mm)	h (mm)	φ
Sample 1 (Al 360 Table salt)	30	8.013	1.320
Sample 2 (Al 360 Himalayan salt)	30	8.016	1.320
Sample 4 (Al 380 Himalayan salt)	30	8.025	1.319
Sample 5 (Al 7075 Table salt)	30	8.019	1.319
Sample 6 (Al 7075 Himalayan salt)	30	8.008	1.321

Using the methodology presented earlier, the stress–strain curves for the remaining specimens were obtained from the recorded load and displacement data Figures 48, 49, 50 and 51 illustrate these curves and show how stress evolves as strain increases up to approximately 75% deformation. These curves capture the entire compressive behaviour of each foam. The curves in each figure represent the same type of aluminium with differences between salt types except in Figure 51, which shows all the curves together.

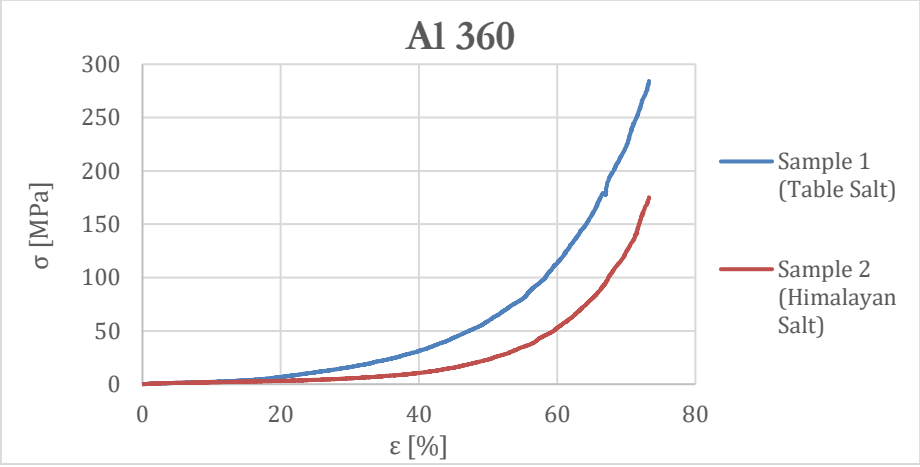

Figure 4.3 - Stress-strain curves for samples 1 and 2 after the cold compression test.

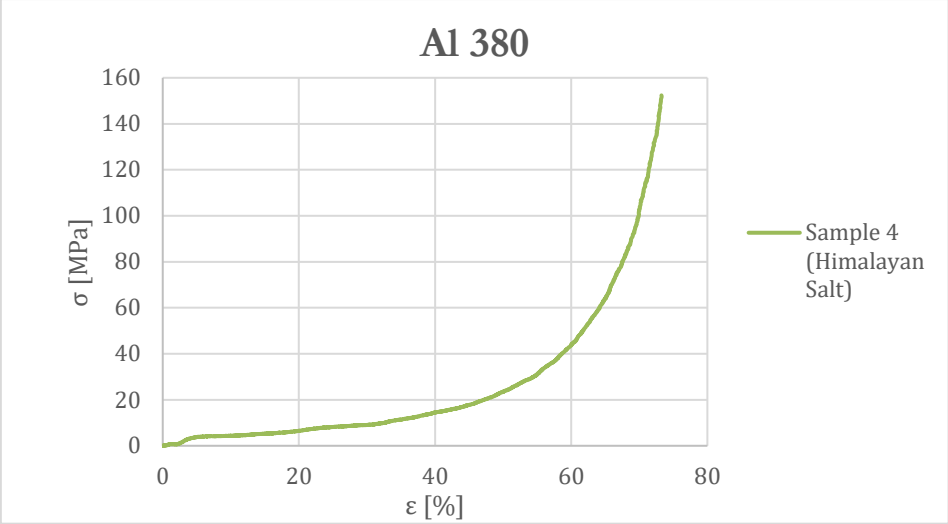

Figure 4.4 - Stress-strain curves for sample 4 after the cold compression test.

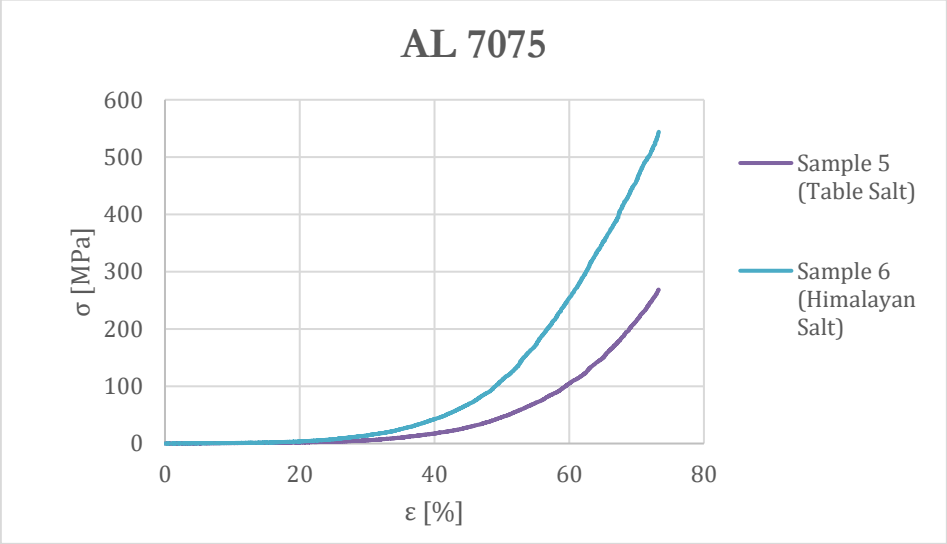

Figure 4.5 - Stress-strain curves for samples 5 and 6 after the cold compression test.

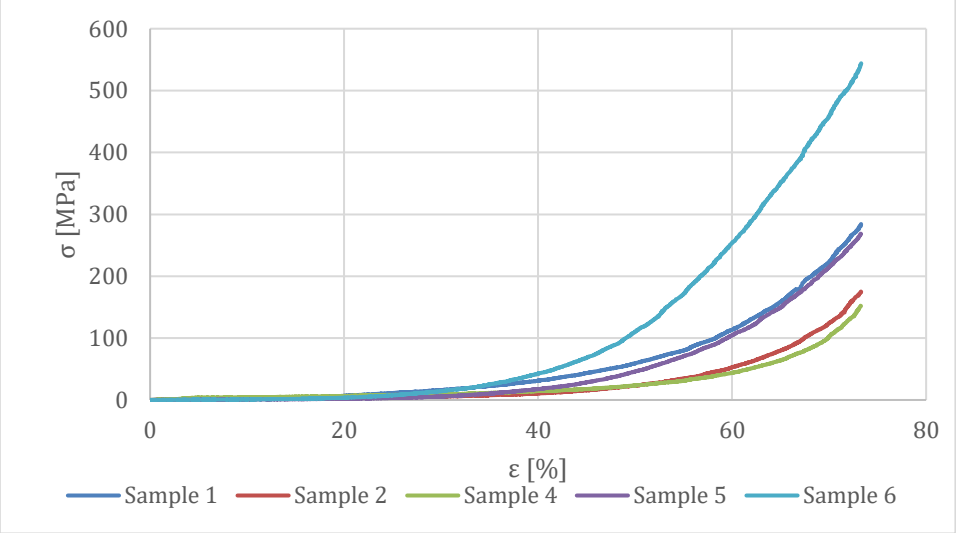

Figure 4.6 - Stress-strain curves for all samples after the cold compression test.

The energy absorption of the foams was determined by integrating the area under the stress–strain curve between ε = 5% and ε = 60%, according to the recommendations of ISO 13314:2011. The lower limit was chosen to eliminate the effects of initial seating and elastic deformation, while the upper limit corresponds to the onset of densification.

The following figures illustrate the compressive behaviour of all samples and the corresponding energy absorption values calculated within the defined strain interval. They compare the differences between samples of the same aluminium type with different types of salt.

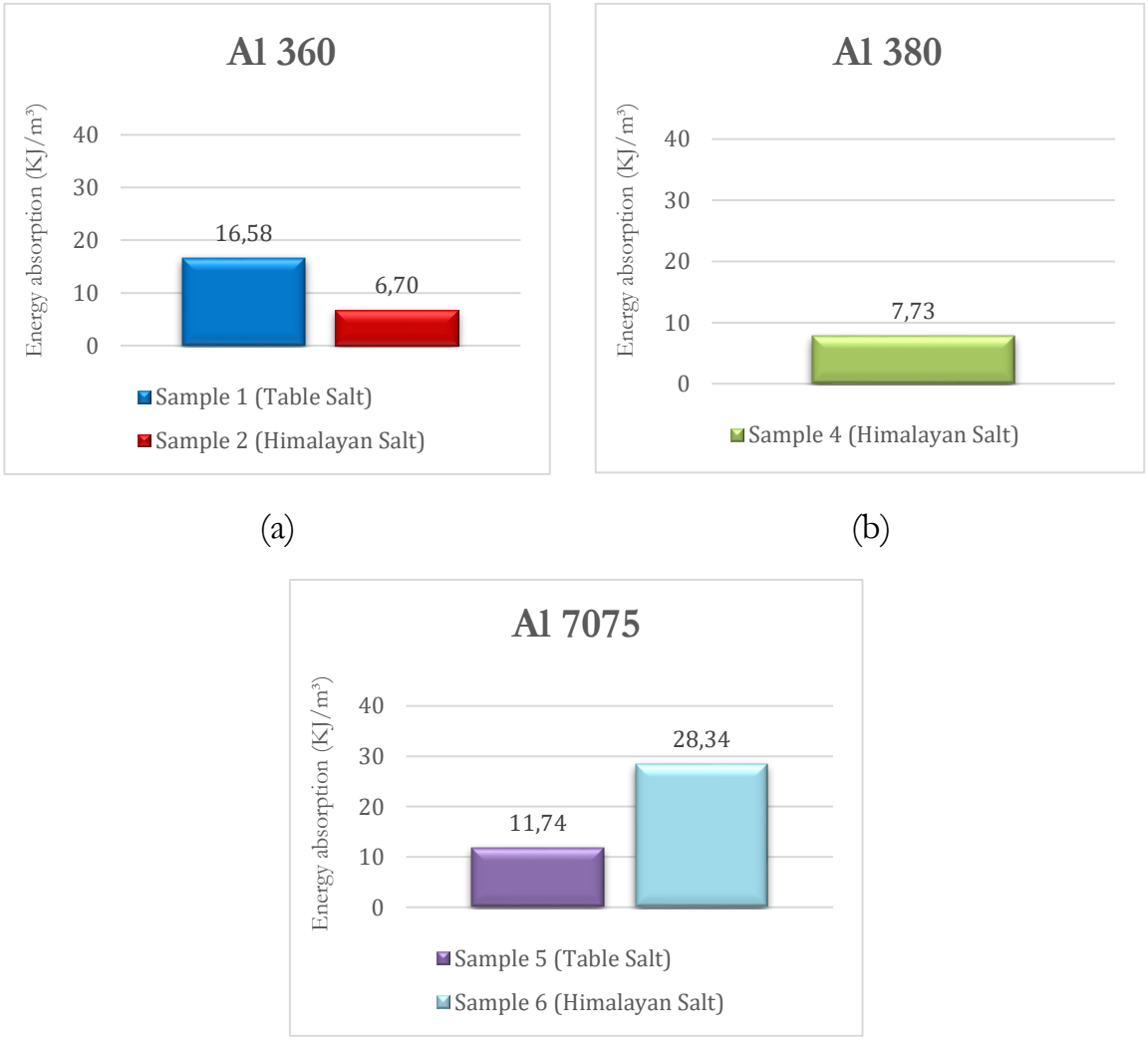

Figure 4.7 - Energy absorption for all samples: (a) - Samples made from Al360 (Table and Himalayan salt, respectively); (b) - Sample made from Al380 (Himalayan salt); (c) - Samples made from Al7075 (Table and Himalayan salt, respectively).

The compressive stress–strain curves of all the specimens show a continuous increase in stress with strain, with no clear plateau. Classical open-cell foams display

a plateau when cell walls collapse sequentially at a constant stress. However, this behaviour is suppressed in the present materials by several microstructural factors:

- Irregular pore geometry, generated by non-uniform salt packing and variable chip compaction, which leads to heterogeneous collapse initiation;
- Variable strut thickness and residual imperfections, which distribute collapse events over a wide strain interval;
- Progressive densification beginning early in deformation, producing a monotonic stress rise.
- Alloy strength effects, particularly in Al 7075, which elevate the stress level throughout the test and hide any plateau behaviour.

Consequently, a distinct plateau stress could not be reliably defined. Instead, energy absorption per unit volume was used as the comparative mechanical parameter.

Energy absorption was calculated as the integral of the stress–strain curve between 5% and 60% of strain (ε). This strain range excludes the initial seating and elastic regions, ending at the start of densification. The results were:

- Sample 1 (Al 360 – Table Salt): 16.58 kJ/m^3
- Sample 2 (Al 360 – Himalayan Salt): 6.70 kJ/m^3
- Sample 4 (Al 380 – Himalayan Salt): 7.73 kJ/m^3
- Sample 5 (Al 7075 – Table Salt): 11.74 kJ/m^3
- Sample 6 (Al 7075 – Himalayan Salt): 28.34 kJ/m^3

The variation in absorbed energy clearly reflects the effects of alloy resistance and pore morphology.

Using the same alloy (Al 360), replacing table salt with Himalayan salt reduced the absorbed energy by almost 60% (from 16.6 kJ/m^3 to 6.7 kJ/m^3). This suggests that Himalayan salt generates a more irregular or less interconnected structure with thinner or weaker supports.

The same trend was observed for Al 7075 foams: the sample containing Himalayan salt (Sample 6) achieved the highest overall energy absorption (28.3 kJ/m^3), which is more than double that of the sample containing table salt (11.7 kJ/m^3). This implies that for this more resistant alloy, the salt's morphology produced a more favourable stress distribution and delayed densification.

Comparing the alloys, Al 7075 foams absorbed significantly more energy than Al 360 and Al 380 in the same deformation range, which is consistent with their higher intrinsic yield strength and strain hardening capacity.

Although all foams have the same nominal porosity (60%), local variations in pore size and structural connectivity, which are inevitable in structures replicated with salt,

have a significant impact on the mechanical response. The absence of a uniform plateau indicates that collapse occurs progressively, with densification occurring at different times in different regions. It was therefore not possible to calculate the plateau stress. However, it was possible to integrate the area under the curve, which provides a more meaningful and reproducible indicator of mechanical performance than reporting a single plateau stress value.

Building upon these results, the next section explores the use of these foams as electrodes in electrocoagulation processes for treating wastewater. Their mechanical robustness, which has been demonstrated previously, supports their electrochemical utilisation, while their morphological characteristics are expected to influence parameters such as current distribution and pollutant removal efficiency. The following results, therefore, focus on evaluating the performance of each foam composition under EC conditions.

4.2 Results and Discussion of the Aluminium Foams in Electrocoagulation Application

This section presents the experimental results obtained during electrocoagulation (EC). The analysis includes an evaluation of the pH level, electrical conductivity, and mass variation of the foams, as well as determining the chemical oxygen demand (COD) removal efficiency and specific energy consumption. Together, these parameters provide a comprehensive assessment of the system's electrochemical performance and its ability to remove pollutants under controlled operating conditions.

4.2.1 pH, Conductivity, and Al Mass

Tables 12 summarise the measured values of pH and electrical conductivity, including the means and standard deviations for both experimental series A and B, while Table 13 presents the foam mass obtained in both experimental runs. These parameters include the initial effluent conditions (pH_i, x_i), the values after acidification (pH_i', x_i'), and the final measurements after electrocoagulation treatment (pH_f, x_f), as well as the initial and final aluminium foam masses (m_i, m_f).

Together, these parameters provide essential insight into the electrochemical behaviour of the system while simultaneously enabling an assessment of the reproducibility of the experimental runs.

The observed variations in pH, conductivity, and foam mass form the basis for subsequent analysis, enabling verification of whether the evolution of these parameters aligns with the expected electrocoagulation behaviour or indicates deviations arising from the specific characteristics of each foam sample.

Table 4.3 - Initial and final mean values of pH and electrical conductivity (Series A and B).

	pH_i	$x_i(mS/cm)$	$pH_{i'}$	$x_{i'}(mS/cm)$	pH_f	$x_f(mS/cm)$
Sample 1	7.19±0.43	3.90±0.04	3.04±0.06	4.70±0.39	5.48±0.28	4.86±0.15
Sample 2	7.26±0.39	3.91±0.04	3.02±0.07	4.61±0.04	5.24±0.14	5.02±0.30
Sample 3	6.98±0.68	3.91±0.07	3.05±0.01	4.60±0.27	4.79±0.72	4.91±0.16
Sample 4	7.30±0.43	3.70±0.28	3.03±0.06	4.68±0.04	5.19±0.11	4.70±0.01

Table 4.4 - Initial and final aluminium foam masses obtained in Series A and B.

	Serie A		Serie B	
	m_i	m_f	m_i	m_f
Sample 1	32.97	33.00	33.00	33.21
Sample 2	36.17	35.84	35.84	35.69
Sample 3	39.01	38.82	38.82	38.75
Sample 4	33.20	33.07	33.07	33.15

In both experimental series, all samples exhibited an increase in pH, with final values ranging from 4.79±0.72 to 5.48±0.28 compared to initial acidified values ranging from 3.02±0.07 to 3.05±0.01.

This rise in pH is typical of electrocoagulation systems, in which the cathodic reduction of water produces hydroxide ions (OH^-) that progressively neutralise the acidified effluent. The increase observed across all samples indicates that both electrodes remained electrochemically active throughout the treatment period, continuously generating hydroxide species.

In terms of electrical conductivity, a general increase was observed following treatment compared to after acidification. This behaviour reflects the generation of ionic species, primarily Al^{3+} and hydrolysed aluminium complexes, arising from anodic dissolution.

In addition to these mechanisms, the rise in conductivity may also be due to the progressive dissolution of residual salt trapped within the foam's internal pores. As anodic dissolution progresses, material is gradually removed from the struts, exposing deeper pore layers that may contain remnants of the original space holder. Once these previously isolated pores come into contact with the effluent, the residual salt begins to dissolve, releasing additional ionic species into the solution. According to Fajardo et al. [90], the dissolution of sodium chloride significantly increases the conductivity of the aqueous medium, thereby providing an additional explanation for the observed increase in conductivity during treatment. This effect is particularly significant for foams produced with less homogeneous salt particles, where incomplete salt removal can result in improved conductivity.

This stability indicates a dynamic equilibrium between the generation and removal of ions: the dissolution of aluminium releases new ions into the solution, while flocculation and the entrapment of pollutants simultaneously remove ionic and colloidal species.

Concerning the foam mass, most samples presented a slight decrease in weight after the experiments, consistent with the expected anodic material loss during electrocoagulation. Although this trend was predominant, a minor mass increase was observed in Sample 1 in both experimental series and in Sample 4 in Series B.

This effect can be attributed either to the retention of coagulant residues, organic matter, or flocs within the foam's open-cell porosity or to the deposition of aluminium hydroxides on the surface, which may locally counteract the expected loss of material due to anodic dissolution. Another possibility is that the drying time was not sufficient.

Overall, the observed changes in pH, conductivity and foam mass are fully consistent with the progression of electrocoagulation reactions, confirming the sustained electrochemical activity of the aluminium foams throughout treatment.

4.2.2 COD Removal Efficiency

The initial and final COD values obtained in both experimental series are presented in Table 14, which correspond to the organic load of the effluent before and after treatment as determined by photometric analysis.

Table 4.5 – Initial and final COD values for experiments A and B and their average.

	COD (mgO_2/L)					
	Experimental Series A		Experimental Series B		Average ± SI	
	Initial Value	Final Value	Initial Value	Final Value	Initial Value	Final Value
Sample 1	1713	349	1807	270	1760 ± 66	309 ± 56
Sample 2	1673	102	1760	124	1717 ± 62	113 ± 15
Sample 3	2043	333	1867	233	1955 ± 124	283 ± 71
Sample 4	1677	292	1697	251	1687 ± 14	271 ± 29

Across both Series A and B, all aluminium foam samples achieved a substantial reduction in COD, decreasing from initial concentrations between 1687±14 and 1955±124 mg O_2/L to final values of 113±15 mg O_2/L and 309±56 mg O_2/L, respectively.

All treated effluents reached values well below the 1000 mg O_2/L pre-treatment limit established by Regulation No. 448/2024, which defines the threshold for discharge into municipal sewer systems. Additionally, Sample 2 achieved final COD

concentrations below 150 mg O_2/L, complying with the direct discharge limit for effluents released into receiving waters, as set out in Decree-Law No. 236/98.

The obtained COD reduction confirms that open-cell aluminium foam electrodes are highly effective at removing organic pollutants, producing effluents that meet industrial pre-treatment standards and, in specific cases, direct discharge standards. This enhanced performance is due to the foam's interconnected porous structure, which increases the effective surface area, improves mass transfer, and promotes the uniform distribution of coagulant species throughout the effluent.

Overall, the treated effluents comply with current Portuguese discharge regulations and demonstrate the suitability of aluminium foam electrodes as an efficient, sustainable alternative for wastewater treatment applications.

4.2.3 Removal Efficiency Percentage

A comparative analysis of Figures 53–56 enables a detailed evaluation of the influence of aluminium grade and salt type on the COD removal behaviour of the foams. Each curve shows the mean values from the two experimental series. To ensure the reliability of these averaged trends, the standard deviation was calculated at every sampling point for each curve. Points that deviated by more than 5% from the mean were treated as outliers and excluded from the plotted datasets. First, the performance of the two alloys synthesised with the same salt is compared, and then the effect of salt type on each aluminium grade is examined individually.

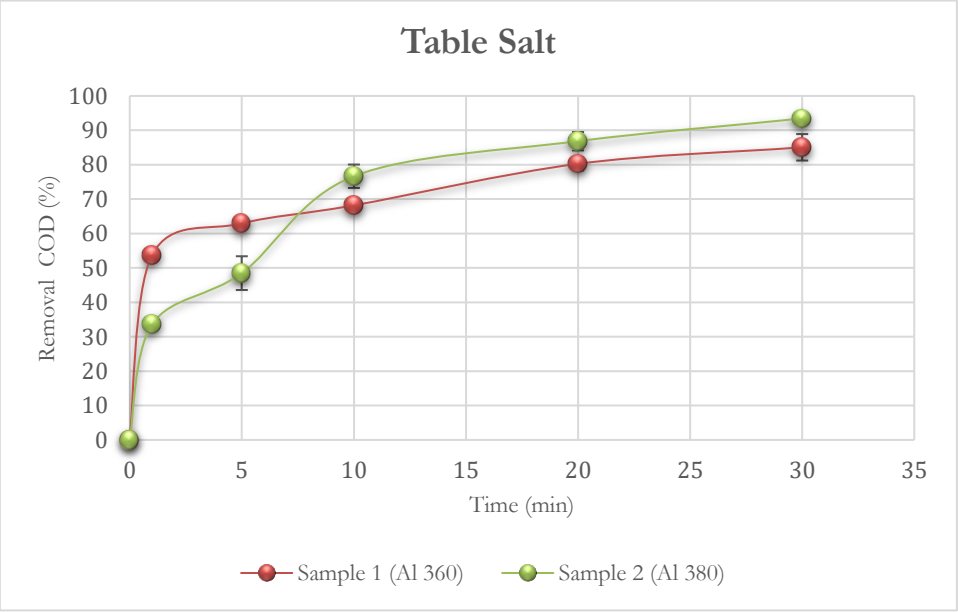

Figure 4.8- Percentage of COD removal comparing the samples with the same type of salt (samples 1 and 2 (Table Salt)), calculated from the means of the two experimental series.

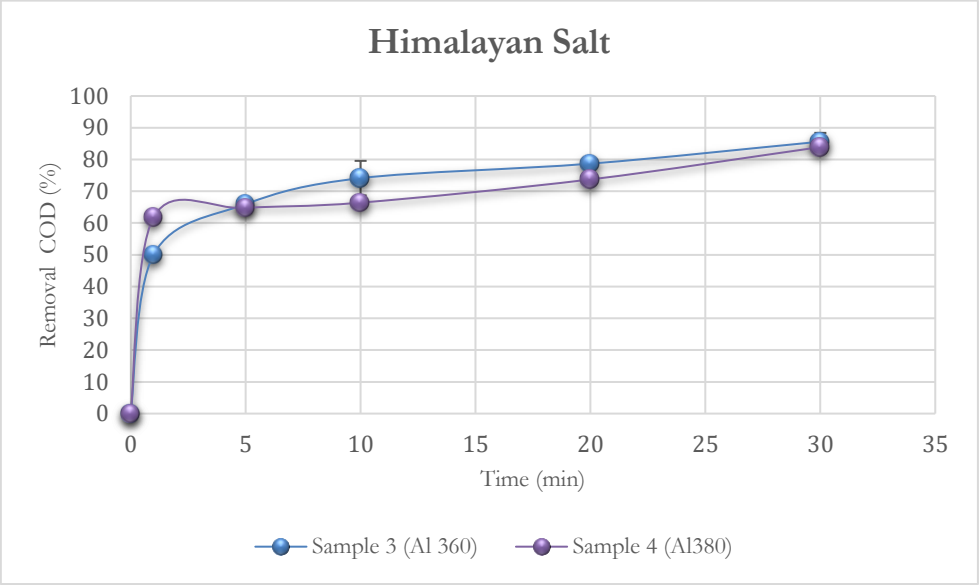

Figure 4.9 - Percentage of COD removal comparing the samples with the same type of salt (samples 3 and 4 (Himalayan Salt)), calculated from the means of the two experimental series.

When comparing foams fabricated using the same space holder (Table Salt), only a slight difference of 8% is observed towards the end of the treatment period (Figure 53). During the first five minutes, the Al360 foam exhibits a faster removal rate, indicating a more rapid initial release of coagulant species. However, between 5 and 10 minutes, this trend reverses and the Al380 foam progressively approaches, and then slightly surpasses, the performance of the Al360 foam. Beyond this point, the two curves follow closely parallel trajectories, culminating in final removal efficiencies above 80%. This confirms the high effectiveness of both alloys in treating the effluent under these conditions.

When Himalayan salt is used as the space holder (Figure 54), the differences between the two aluminium grades become less pronounced still. The final removal values at 30 minutes are essentially identical, with the Al380 foam exhibiting a modest advantage of approximately 9% in the first minute. This disparity disappears rapidly and the two alloys converge to produce nearly indistinguishable removal profiles for the remainder of the test. Once again, both materials achieve consistently high removal efficiencies, indicating that the choice of alloy has only a minor influence when combined with this particular space holder.

The small variations observed between Al360 and Al380 across both salt types can be explained in light of their compositional and microstructural characteristics. Since the electrical conductivities of the two grades are very similar (see Table 5), conductivity can reasonably be excluded as a determining factor in the observed behaviour. Instead, subtle compositional differences, most notably the higher levels of Cu and Zn in Al380, may introduce localised intermetallic phases or micro-galvanic cells, which could slightly modify the anodic dissolution kinetics. Fajardo et al. reported that Zn-based species exhibit a particular affinity for organic phenolic matter. Although the amount of Zn in Al380 is minimal, it may still contribute

marginally to the differences observed between the two alloys in the early stages [9]. However, this effect is expected to be limited and should be considered a conceptual framework rather than direct evidence of Zn-driven removal mechanisms.

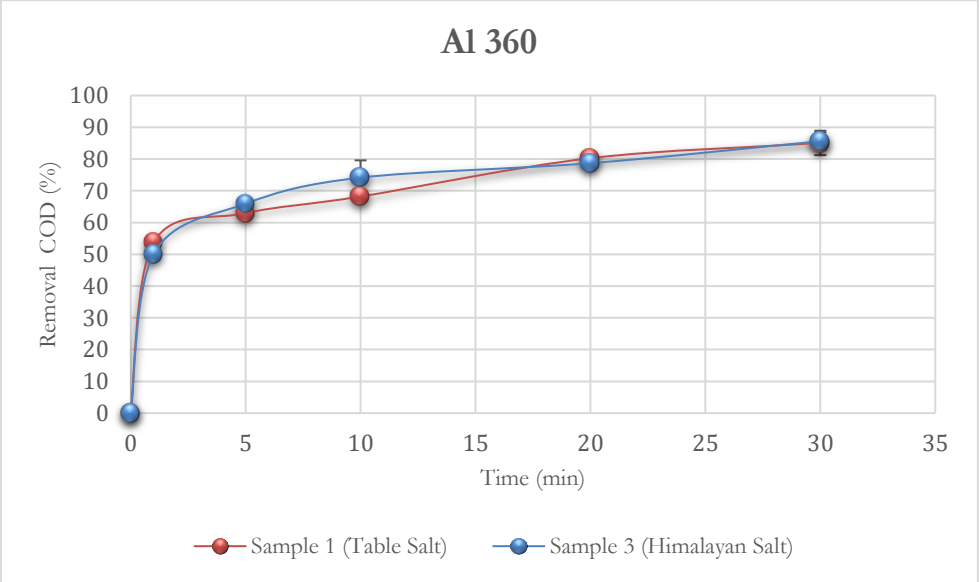

Figure 4.10 - Percentage of COD removal comparing the samples with the same type of aluminium (samples 1 and 3 (Al 360)), calculated from the means of the two experimental series.

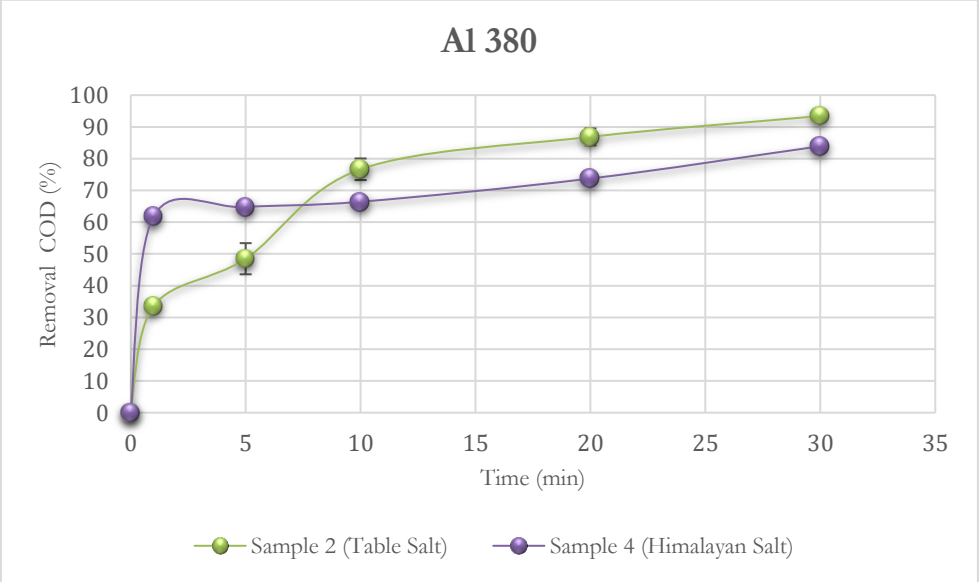

Figure 4.11 - Percentage of COD removal comparing the samples with the same type of aluminium (samples 2 and 4 (Al 380)), calculated from the means of the two experimental series.

Examining the effect of salt type within each aluminium grade reveals that the Al360 foams (Figure 55) exhibit almost indistinguishable behaviour. Both the table salt and Himalayan salt specimens follow practically identical removal trajectories throughout the entire treatment period. The final efficiencies differ by less than one percentage point, suggesting that the morphology induced by the two salts did not significantly impact the electrocoagulation performance of this alloy.

In contrast, the Al380 foams (Figure 56) display more pronounced differences. While both samples achieve high removal efficiencies, the table salt foam achieves approximately 93% removal after 30 minutes, whereas the Himalayan salt foam reaches only about 84%. Interestingly, the behaviour in the first few minutes is reversed: between 0 and 5 minutes, the Himalayan salt foam shows a sharper initial increase in removal than the table salt foam. However, this advantage is short-lived. Between 5 and 10 minutes, the trend inverts, with the table salt sample overtaking the Himalayan salt sample and maintaining consistently higher values thereafter.

A plausible explanation for this behaviour lies in the distinctive pore structures generated by each type of salt. Table salt typically produces smaller, more numerous pores, which collectively provide a larger real surface area for anodic dissolution and floc formation. In contrast, Himalayan salt, which contains larger grains, generates fewer but larger cavities, thereby reducing the total internal surface area available for reaction.

However, it is important to emphasise that these observations remain preliminary. As discussed in the section on mechanical characterisation, one intrinsic limitation of salt-replicated foams is their heterogeneous porosity. Even when produced under identical conditions, two nominally identical specimens may exhibit different pore architectures and distinct distributions of strut thicknesses. This variability inevitably influences surface exposure and, therefore, the electrocoagulation dynamics. Accordingly, the variations observed for the Al380 samples may reflect not only the intrinsic influence of salt type, but also subtle differences arising during foam fabrication.

4.2.4 Electrical Voltage and Energy Consumption

Tables 15 and 16 summarise the voltage values recorded for all samples throughout the electrocoagulation process during both experimental runs. These data were collected at predefined time intervals to provide an overview of the system's electrical behaviour during operation.

Table 4.6 - Voltage values for Experimental Series A.

	Sample 1 (V)	Sample 2 (V)	Sample 3 (V)	Sample 4 (V)
T_0	6.0	5.9	7.1	7.6
T_1	5.7	5.0	6.0	7.4
T_5	5.5	4.7	5.7	6.5
T_{10}	5.4	4.5	5.7	6.1
T_{20}	5.4	4.3	5.6	5.7
T_{30}	5.1	4.3	5.5	5.7
Average	5.5	4.6	5.7	6.3

Table 4.7 - Voltage values for Experimental Series B.

	Sample 1 (V)	Sample 2 (V)	Sample 3 (V)	Sample 4 (V)
T_0	6.0	5.5	6.0	6.7
T_1	5.8	5.3	5.3	6.0
T_5	5.9	5.3	5.1	5.8
T_{10}	5.9	5.3	5.0	5.7
T_{20}	5.8	5.0	4.8	5.6
T_{30}	5.7	5.0	4.8	5.6
Average	5.9	5.3	5.1	5.8

The voltage profiles recorded during electrocoagulation revealed stable cell operation for all samples, with a gradual decrease in potential over time. This behaviour is consistent with the progressive reduction in ionic strength and the formation of conductive aluminium hydroxide flocs. The initial voltages ranged from 5.9 to 7.6 V and decreased to final values between 4.3 to 5.7 V. This confirms that the system remained electrochemically stable throughout the treatment, with no evidence of passivation or erratic behaviour.

A slight deviation from this general trend was observed in Sample 1 (Experimental series B), where the potential increased marginally from 5.8 V to 5.9 V between T_1 and T_5. This variation is most likely associated with the adjustments made during the experiment, as withdrawing 50 mL of liquid progressively reduced the effluent volume and required the electrodes to be repositioned manually. Any minor inaccuracy in this adjustment, or any lack or insufficient insulation of the cell, can momentarily alter the immersion depth, leading to small changes in voltage. Once the electrode position was stabilised, the potential returned to the expected decreasing trend, consistent with the behaviour observed across all other samples.

Figures 57 and 58 present the calculated specific energy consumption (kWh/m^3) for each foam configuration, based on mean values obtained from two experimental series. Each figure contains two subplots labelled (a) and (b) that enable the direct comparison of the influence of aluminium grade and salt type. Figure 57(a) compares Samples 1 and 2, which were both manufactured using table salt but with different aluminium alloys. Figure 57(b) presents the corresponding comparison for samples produced using Himalayan salt. Similarly, Figures 58(a) and 58(b) compare samples 1 and 3 and samples 2 and 4, respectively, enabling the influence of salt type to be assessed for each aluminium grade (Al360 and Al380).

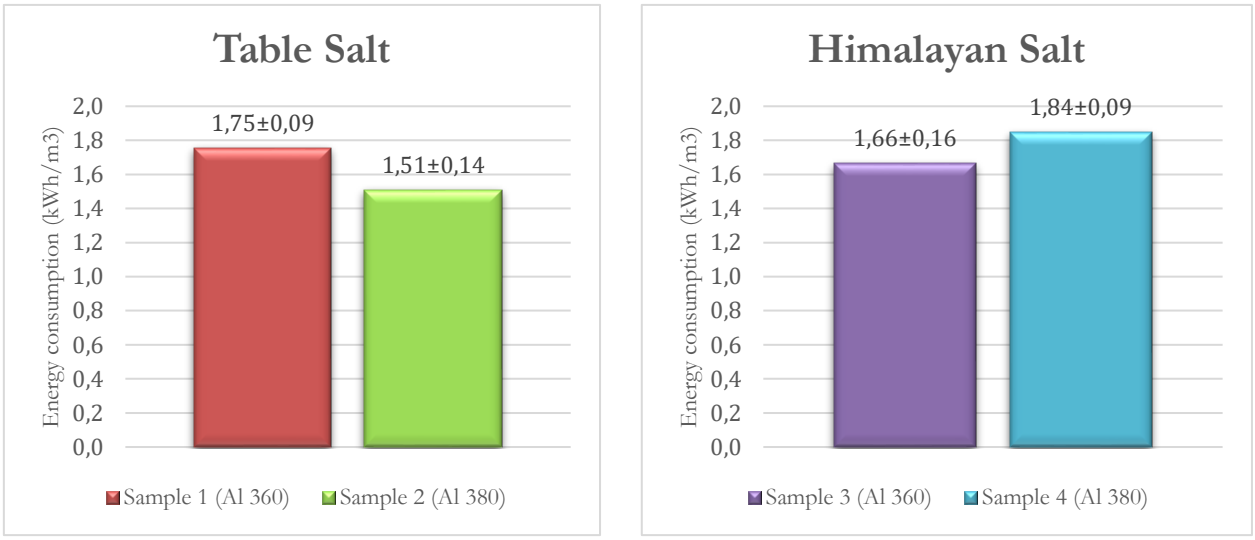

(a) (b)

Figure 4.12 - Energy consumption: (a)- Samples with Table salt; (b)- Samples with Himalayan salt.

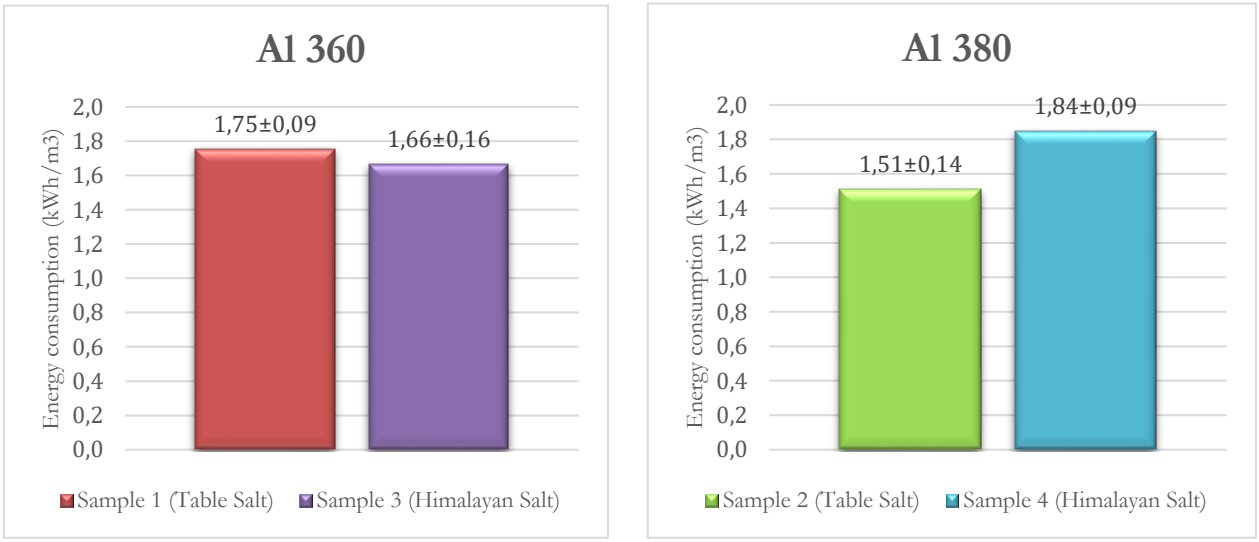

(a) (b)

Figure 4.13 - Energy consumption: (a)-Samples with Al 360; (b)- Samples with Al 380.

When the foams were produced using table salt (Figure 57-(a)), both alloys exhibited broadly similar energy requirements. However, the Al380 foam showed slightly lower consumption (1.51 ± 0.14 kWh/m³), compared to the Al360 foam (1.75 ± 0.09 kWh/m³). Therefore, under these conditions, Al380 appears marginally more energy efficient.

In contrast to previously observed behaviour, the foams synthesised with Himalayan salt (Figure 57-(b)) exhibited an opposite trend. In this case, the values remained relatively close, ranging from 1.66 ± 0.16 kWh/m³ for Al360 to 1.84 ± 0.09 kWh/m³ for Al380. This indicates that slightly more energy was required for the Al380 foam.

For Al360 (Figure 58-(a), the difference between table salt and Himalayan salt is negligible, indicating that the change in pore morphology induced by the two salts does not substantially affect this alloy's electrical behaviour during electrocoagulation. In contrast, the Al380 foams (Figure 58-(b)) display a more noticeable distinction: the foam made with table salt consumes 1.51 ± 0.14 kWh/m³, whereas the foam made with Himalayan salt requires 1.84 ± 0.09 kWh/m³. This suggests that the Al380 alloy is more sensitive to variations in porosity and internal morphology generated by different space holders.

These trends are consistent with the final conductivity values reported in Table 12, which directly influence the voltage required to maintain the applied current. As previously discussed, the dissolution of trapped salt residues from the internal pores increases the ionic concentration of the wastewater, thereby raising its electrical conductivity. According to Ohm's law, higher conductivity reduces overall cell resistance, lowering the operating voltage and, consequently, the specific energy consumption. This explains why Sample 2, which had the highest final conductivity, also exhibited one of the lowest energy consumption values.

In summary, systems operating in more conductive media demonstrate reduced energy demand, whereas foams associated with lower conductivities require higher voltages and thus have a higher specific energy consumption. Therefore, the observed differences reflect not only the alloy composition but also the extent to which residual salts within the foam structure enhance the electrical conductivity of the treated effluent during operation.

The combined analysis of removal efficiency and energy demand clearly shows that Sample 2 is the most advantageous configuration overall. It delivers the highest pollutant removal performance while maintaining the lowest specific energy consumption, and benefits from the practical and economic advantages of using table salt as a space holder. For these reasons, Sample 2 stands out as the most suitable option for future electrocoagulation studies and potential process optimisation.

5 CONCLUSION

This dissertation evaluated the potential of aluminium foams produced from recycled machining chips for use as mechanically robust and electrochemically active electrodes in wastewater treatment via electrocoagulation. Initially, eight foams were fabricated using four aluminium alloys and two space-holder salts. However, only six of these demonstrated sufficient structural integrity for mechanical testing. The Al6082 specimens fractured completely during sectioning and were excluded as a result, highlighting the sensitivity of foam formation to alloy ductility, chip work-hardening, and internal inclusions.

The remaining foams exhibited interconnected porosity consistent with successful replication. Their mechanical response reflected the combined influence of alloy strength and pore morphology, with the latter proving to be particularly significant. Although classical plateau behaviour was absent due to heterogeneous cell geometry and variable strut thickness, all usable samples sustained large deformations with progressively increasing stress. Energy absorption between 5% and 60% strain revealed clear performance trends: Sample 6 (Al7075–Himalayan salt) achieved the highest value, absorbing 28.34 kJ/m³, while Sample 2 (Al360–Himalayan salt) corresponded to the lowest. These results highlight the reinforcing effect of the stronger Al7075 matrix and the significant impact of granulation on structural continuity.

Electrocoagulation experiments were conducted using foams produced from Al360 and Al380 alloys, along with Table salt and Himalayan salt. All four samples exhibited consistent anodic activity, with progressive pH neutralisation and stable conductivity. Notably, the COD removal performance was impressive, with initial values ranging from 1670 to 2040 mg O_2/L being reduced to 102–333 mg O_2/L. All treated effluents met Portuguese discharge standards for sewer discharge, and one even fell below 150 mg O_2/L. In terms of COD removal, the Al380 foam produced with table salt delivered the best overall performance, whereas Al360 showed marginally superior behaviour when manufactured with Himalayan salt. These variations reflect subtle interactions between alloy composition and pore geometry, particularly the influence of pore size distribution on effective surface area and mass-transfer kinetics.

Although some variation between samples was observed, the specific energy consumption remained comparatively low for all foams. This behaviour is consistent with the conductivity evolution measured during electrocoagulation: as the residual salt trapped within the foam pores dissolved into the effluent, the ionic strength of the medium increased. The resulting rise in conductivity lowered the cell's electrical resistance, reducing the operating voltage required to sustain the imposed current. Consequently, the overall energy demand remained modest for all configurations, reflecting the morphological characteristics of the foams and the beneficial

contribution of residual salts to maintaining favourable electrical conditions throughout the treatment process.

Overall, this study demonstrates that aluminium foams produced from recycled chips can operate effectively as EC electrodes while retaining the mechanical robustness required for sacrificial use. The results confirm the feasibility of converting machining waste into functional porous electrodes, supporting both material circularity and sustainable water-treatment practices.

Future developments may focus on refining the mixing and replication steps to enhance pore uniformity, thereby reducing sample-to-sample variability. Extending the concept to chips from other metals, such as steel, copper or brass, could broaden the technological relevance of this approach. From an electrocoagulation perspective, exploring different electrode spacings, current densities or polarity-reversal strategies would provide deeper insight into dissolution dynamics and long-term stability. Extended-duration testing is also recommended to evaluate durability, fouling behaviour and operational consistency under realistic treatment conditions.

References:

[1] - You, X., Xing, Z., Jiang, S., Zhu, Y., Lin, Y., Qiu, H., ... & Chen, Y. (2024). A review of research on aluminium alloy materials in structural engineering. Developments in the built environment, 17, 100319.

[2] - Allwood, J. M., Cullen, J. M., Carruth, M. A., Cooper, D. R., McBrien, M., Milford, R. L., ... & Patel, A. C. (2012). Sustainable materials: with both eyes open (Vol. 2012). Cambridge, UK: UIT Cambridge Limited.

[3] - Kumar, N., & Bharti, A. (2021). Review on powder metallurgy: A novel technique for recycling and foaming of aluminium-based materials. Powder Metallurgy and Metal Ceramics, 60(1), 52-59.

[4] - Raabe, D. (2023). The materials science behind sustainable metals and alloys. Chemical reviews, 123(5), 2436-2608.

[5] - Banhart, J. (2006). Metal foams: production and stability. Advanced engineering materials, 8(9), 781-794.

[6] - Banhart, J. (2001). Manufacture, characterisation and application of cellular metals and metal foams. Progress in materials science, 46(6), 559-632.

[7] - Wan, T., Liu, Y., Zhou, C., Chen, X., & Li, Y. (2021). Fabrication, properties, and applications of open-cell aluminium foams: A review. Journal of Materials Science & Technology, 62, 11-24.

[8] - Surace, R., De Filippis, L. A. C., Ludovico, A. D., & Boghetich, G. (2009). Influence of processing parameters on aluminium foam produced by space holder technique. Materials & Design, 30(6), 1878-1885.

[9] - Rincón, G. J., & La Motta, E. J. (2014). Simultaneous removal of oil and grease, and heavy metals from artificial bilge water using electro-coagulation/flotation. Journal of Environmental management, 144, 42-50.

[10] - Mollah, M. Y. A., Schennach, R., Parga, J. R., & Cocke, D. L. (2001). Electrocoagulation (EC)—science and applications. Journal of hazardous materials, 84(1), 29-41.

[11] - Holt, P. K. (2002). Electrocoagulation: unravelling and synthesising the mechanisms behind a water treatment process.

[12] - Burson, E. (n.d.). What is the Chemical Oxygen Demand (DQO)? PRODOS. Retrieved November 7, 2025, from https://prodos.es/en/what-is-the-chemical-oxygen-demand-dqo/

[13] - Mazzolani, F. M. (Ed.). (2014). Aluminium structural design (Vol. 443). Springer.

[14] - Raabe, D., Tasan, C. C., & Olivetti, E. A. (2019). Strategies for improving the sustainability of structural metals. Nature, 575(7781), 64-74.

[15] - Daehn, K., Basuhi, R., Gregory, J., Berlinger, M., Somjit, V., & Olivetti, E. A. (2022). Innovations to decarbonize materials industries. Nature Reviews Materials, 7(4), 275-294.

[16] - The International Aluminium Institute (IAI). Current Statistics. https://international-aluminium.org.

[17] - Jozić, S., Lela, B., Krolo, J., & Jakovljević, S. (2023). Production of open-cell metal foams by recycling of aluminium alloy chips. Materials, 16(11), 3930.

[18] - Zheng, Y. (2019). Biological design of materials. Materials Today, 27-97.

[19] - Kriszt, B., Martin, U., Mosler, U., Maire, E., Degischer, H. P., & Kottar, A. (2002). Characterization of cellular metals. Handbook of cellular metals: production, processing, applications, 127-178.

[20] - Hassan, A., & Alnaser, I. A. (2024). A review of different manufacturing methods of metallic foams. ACS omega, 9(6), 6280-6295.

[21] - Konstantinidis, I. C., Paradisiadis, G., & Tsipas, D. N. (2009). Analytical models for the mechanical behavior of closed and open-cell Al foams. Theoretical and applied fracture mechanics, 51(1), 48-56.

[22] - Simone, A. E., & Gibson, L. J. (1998). Effects of solid distribution on the stiffness and strength of metallic foams. Acta materialia, 46(6), 2139-2150.

[23] - Jang, W. Y., Kyriakides, S., & Kraynik, A. M. (2010). On the compressive strength of open-cell metal foams with Kelvin and random cell structures. International Journal of Solids and Structures, 47(21), 2872-2883.

[24] - Ashby, M. F. (2000). Metal foams: a design guide. Elsevier.

[25] - Patel, N., Mittal, G., Agrawal, M., & Pradhan, A. K. (2024). Aluminum foam production, properties, and applications: a review. International Journal of Metalcasting, 18(3), 2181-2198.

[26] - Surace[1], R., & De Filippis, L. A. (2010). Investigation and comparison of aluminium foams manufactured by different techniques. Advanced knowledge application in practice, 95.

[27] - Singh, S., & Bhatnagar, N. (2018). A survey of fabrication and application of metallic foams (1925–2017). Journal of Porous Materials, 25(2), 537-554.

[28] - Babcsán, N., Banhart, J., & Leitlmeier, D. (2003, November). Metal foams–manufacture and physics of foaming. In Proceedings of the International Conference Advanced Metallic Materials (Vol. 5, p. 15).

[29] - Banhart, J. (2000). Manufacturing routes for metallic foams. Jom, 52(12), 22-27.

[30] - Ashby, M. F., Evans, A., Fleck, N. A., Gibson, L. J., Hutchinson, J. W., Wadley, H. N. G., & Delale, F. (2001). Metal foams: a design guide. Applied Mechanics Reviews, 54(6), B105-B106.

[31] - Baumeister, J., & Schrader, H. (1991). Methods for manufacturing foamable metal bodies. German Patent DE, 41(01), 630.

[32] - Bauer, B., Kralj, S., & Bušić, M. (2013). Production and application of metal foams in casting technology. Tehnicki vjesnik, 20(6), 1095-1102.

[33] - Amjad, S. (2001). Thermal conductivity and noise attenuation in aluminium foams. Adissertation submitted for the degree of Master of Philosophy in Materials Modelling at the University of Cambridge, 3-7.

[34] - Soni, B., & Biswas, S. (2017). Mass-scale processing of open-cell metallic foams by pressurized casting method. Journal of Porous Materials, 24(1), 29-37.

[35] - Kulshreshtha, A., & Dhakad, S. K. (2020). Preparation of metal foam by different methods: A review. Materials Today: Proceedings, 26, 1784-1790.

[36] - Rajak, D. K., & Gupta, M. (2020). An insight into metal based foams. Singapore, Springer, DOI, 10, 978-981.

[37] - Ashby, M. F. (2006). The properties of foams and lattices. Philosophical Transactions of the Royal Society A: Mathematical, Physical and Engineering Sciences, 364(1838), 15-30.

[38] - Lopatnikov, S. L., Gama, B. A., Haque, M. J., Krauthauser, C., Gillespie Jr, J. W., Guden, M., & Hall, I. W. (2003). Dynamics of metal foam deformation during Taylor cylinder–Hopkinson bar impact experiment. Composite Structures, 61(1-2), 61-71.

[39] - Tan, P. J., Harrigan, J. J., & Reid, S. R. (2002). Inertia effects in uniaxial dynamic compression of a closed cell aluminium alloy foam. Materials science and technology, 18(5), 480-488.

[40] - Tan, P. J., Reid, S. R., & Harrigan, J. J. (2012). On the dynamic mechanical properties of open-cell metal foams–A re-assessment of the 'simple-shock theory'. International Journal of Solids and Structures, 49(19-20), 2744-2753.

[41] - Lopatnikov, S. L., Gama, B. A., Haque, M. J., Krauthauser, C., & Gillespie Jr, J. W. (2004). High-velocity plate impact of metal foams. International Journal of impact engineering, 30(4), 421-445.

[42] - Davis, J. R. (Ed.). (2004). Tensile testing. ASM international.

[43] - Han, F., Zhu, Z., Liu, C., & Gao, J. (1999). Damping behavior of foamed aluminum. Metallurgical and Materials Transactions A, 30(13), 771-776.

[44] - Yu, C. J., & Banhart, J. (1997, October). Mechanical properties of metallic foams. In Proceedings of Fraunhofer USA Metal Foam Symposium, Stanton, Delaware (pp. 7-8).

[45] - Han, F., Zhu, Z., Liu, C., & Gao, J. (1999). Damping behavior of foamed aluminum. Metallurgical and Materials Transactions A, 30(13), 771-776.

[46] - Liang, L. S., Wu, X. L., Ma, N. N., Du, J. J., & Liu, M. B. (2018, November). The sound absorption properties comparison of metal foams and flexible cellular materials. In Materials Science Forum (Vol. 933, pp. 357-366). Trans Tech Publications Ltd.

[47] - Arjunan, A., Baroutaji, A., Praveen, A. S., Olabi, A. G., & Wang, C. J. (2019). Acoustic performance of metallic foams.

[48] - Lu, T. J., Hess, A., & Ashby, M. F. (1999). Sound absorption in metallic foams. Journal of applied physics, 85(11), 7528-7539.

[49] - Cao, L., Fu, Q., Si, Y., Ding, B., & Yu, J. (2018). Porous materials for sound absorption. Composites Communications, 10, 25-35.

[50] - Han, F., Seiffert, G., Zhao, Y., & Gibbs, B. (2003). Acoustic absorption behaviour of an open-celled aluminium foam. Journal of Physics D: Applied Physics, 36(3), 294.

[51] - Haijun, Y., Guangchun, Y., & Yan, C. (2008). Influence factors of sound absorption properties of closed-cell aluminium foam [J]. The Chinese Journal of Nonferrous Metals, 18(08), 1487-1491.

[52] - Bergman, T. L., Lavine, A. S., Incropera, F. P., & DeWitt, D. P. (2011). Introduction to heat transfer. John Wiley & Sons.

[53] - Baloyo, J. M. (2017). Open-cell porous metals for thermal management applications: fluid flow and heat transfer. Materials Science and Technology, 33(3), 265-276.

[54] - Lu, T. J., Stone, H. A., & Ashby, M. F. (1998). Heat transfer in open-cell metal foams. Acta materialia, 46(10), 3619-3635.

[55] - Hwang, J. J., Hwang, G. J., Yeh, R. H., & Chao, C. H. (2002). Measurement of interstitial convective heat transfer and frictional drag for flow across metal foams. J. Heat Transfer, 124(1), 120-129.

[56] - Seyf, H. R., & Layeghi, M. (2010). Numerical analysis of convective heat transfer from an elliptic pin fin heat sink with and without metal foam insert.

[57] - Holman, J. P. (1989). Heat Transfer–a Modern Approach.

[58] - Ding, X. R., Lu, L. S., Chen, C., He, Z. S., & Ou, D. S. (2011). Heat transfer enhancement by using four kinds of porous structures in a heat exchanger. Applied Mechanics and Materials, 52, 1632-1637.

[59] - Kim, A., Hasan, M. A., Nahm, S. H., & Cho, S. S. (2005). Evaluation of compressive mechanical properties of Al-foams using electrical conductivity. Composite Structures, 71(2), 191-198.

[60] - Ma, X., Peyton, A. J., & Zhao, Y. Y. (2005). Measurement of the electrical conductivity of open-celled aluminium foam using non-contact eddy current techniques. Ndt & E International, 38(5), 359-367.

[61] - Sevostianov, I., Kováik, J., & Simaník, F. (2002). Correlation between elastic and electric properties for metal foams: theory and experiment. International Journal of Fracture, 114(4), 23-28.

[62] - Dharmasena, K. P., & Wadley, H. N. G. (2002). Electrical conductivity of open-cell metal foams. Journal of materials research, 17(3), 625-631.

[63] - Davies, G. J., & Zhen, S. (1983). Metallic foams: their production, properties and applications. Journal of Materials science, 18(7), 1899-1911.

[64] - Singh, S., & Bhatnagar, N. (2018). A survey of fabrication and application of metallic foams (1925–2017). Journal of Porous Materials, 25(2), 537-554.

[65] - García-Moreno, F. (2016). Commercial applications of metal foams: Their properties and production. Materials, 9(2), 85.

[66] - Yin, H., Chen, C., Hu, T., & Wen, G. (2018). Optimisation for bending crashworthiness of functionally graded foam-filled cellular structure. International Journal of Crashworthiness, 23(4), 446-460.

[67] - Walther, G., Gaitzsch, U., Büttner, T., Kieback, B., Weissgaerber, T., Kolvenbach, R., & Lincke, M. (2017). Applications of metal foam as catalyst carrier. Proceedings of the Euro PM2017, Milan, Italy, 1-5.

[68] - Matsushita, T., Fujibayashi, S., & Kokubo, T. (2017). Titanium foam for bone tissue engineering. In Metallic Foam Bone (pp. 111-130). Woodhead Publishing.

[69] - Zhao, C. Y., Kim, T., Lu, T. J., & Hodson, H. P. (2001). Thermal transport phenomena in porvair metal foams and sintered beds. Final Report, August.

[70] - Arenas, L. F., De León, C. P., & Walsh, F. C. (2019). Three-dimensional porous metal electrodes: Fabrication, characterisation and use. Current Opinion in Electrochemistry, 16, 1-9.

[71] - Castillo, Y. M. A., Adjez, Y., Ccana, V. R. J., Cerrón-Calle, G. A., Garcia-Segura, S., Gómez, A. L. R. T., & Sánchez-Sánchez, C. M. (2024). Benchmarking three-dimensional metal foam electrodes for the electrochemical reduction of nitrate. Journal of Electroanalytical Chemistry, 968, 118499.

[72] - Sharaj Sharifi, N., & Karimi-Jashni, A. (2023). Development and application of novel high throughput metal waste chips and foam electrodes for electrocoagulation treatment of graywater. Environmental Technology, 44(4), 528-539.

[73] - Jang, G. G., Zhang, Y., Keum, J. K., Bootwala, Y. Z., Hatzell, M. C., Jassby, D., & Tsouris, C. (2022). Neutron tomography of porous aluminium electrodes used in electrocoagulation of groundwater. Frontiers in Chemical Engineering, 4, 1046627.

[74] - Kim, K., Castillo, C., Jang, G. G., Zhang, Y., Tsouris, C., & Chellam, S. (2024). Porous Iron Electrodes Reduce Energy Consumption During Electrocoagulation of a Virus Surrogate: Insights into Performance Enhancements Using Three-Dimensional Neutron Computed Tomography. ACS Es&t Engineering, 4(10), 2573-2584.

[75] - Crini, G., & Lichtfouse, E. (2019). Advantages and disadvantages of techniques used for wastewater treatment. Environmental chemistry letters, 17(1), 145-155.

[76] - Nahiun, K. M., Sarker, B., Keya, K. N., Mahir, F. I., Shahida, S., & Khan, R. A. (2021). A review on the methods of industrial waste water treatment. Scientific Review, 7(3), 20-31.

[77] - Ranade, V. V., & Bhandari, V. M. (2014). Industrial wastewater treatment, recycling and reuse. Butterworth-Heinemann.

[78] - Kabdaşlı, I., Arslan-Alaton, I., Ölmez-Hancı, T., & Tünay, O. J. E. T. R. (2012). Electrocoagulation applications for industrial wastewaters: a critical review. Environmental Technology Reviews, 1(1), 2-45.

[79] - Ozyonar, F., & Karagozoglu, B. (2011). Operating cost analysis and treatment of domestic wastewater by electrocoagulation using aluminium electrodes. Pol. J. Environ. Stud, 20(1), 173.

[80] - Koyuncu, S., & Arıman, S. (2020). Domestic wastewater treatment by real-scale electrocoagulation process. Water Science and Technology, 81(4), 656-667.

[81] - Arabian, D. (2021). Optimization of electrocoagulation system for municipal wastewater treatment. Desalination and Water Treatment, 217, 145-158.

[82] - Gatsios, E., Hahladakis, J. N., & Gidarakos, E. (2015). Optimization of electrocoagulation (EC) process for the purification of a real industrial wastewater from toxic metals. Journal of Environmental Management, 154, 117-127.

[83] - Dalvand, A., Gholami, M., Joneidi, A., & Mahmoodi, N. M. (2011). Dye removal, energy consumption and operating cost of electrocoagulation of textile wastewater as a clean process. Clean–Soil, Air, Water, 39(7), 665-672.

[84] - Asselin, M., Drogui, P., Benmoussa, H., & Blais, J. F. (2008). Effectiveness of electrocoagulation process in removing organic compounds from slaughterhouse wastewater using monopolar and bipolar electrolytic cells. Chemosphere, 72(11), 1727-1733.

[85] - Gabrian International. (n.d.). A360 aluminum alloy: Benefits, applications and comparison with A380. Retrieved October 27, 2025, from https://gabrian.com/a360-aluminum-alloy/

[86] - Thyssenkrupp Materials (UK) Ltd. (n.d.). Aluminium alloy 6082. Retrieved October 27, 2025, from https://www.thyssenkrupp-materials.co.uk/aluminium-6082.html

[87] - Thames Stockholders Ltd. (n.d.). Aluminium 7075 – Technical datasheet. Retrieved October 27, 2025, from https://www.thamesstock.com/assets/pdf/aluminium/7075-aluminiumdatasheet.pdf

[88] - Lonergan, J., Goncharov, V., Swinhart, M., Makovsky, K., Rollog, M., McNamara, B., ... & Paviet, P. (2023). Thermodynamic investigation of the NaCl-KCl salt system from 25 to 950° C. Journal of Molecular Liquids, 391, 122591.

[89] - Vicetto, M. A. (2025, March). Optimization of Wastewater Treatment from the Cork Industry by Electrocoagulation Using Metallic Residues as Electrodes. Internship Report for the Bachelor's Degree in Bioengineering – Biological Engineering Branch, Coimbra Institute of Engineering (ISEC), unpublished.

[90] - Fajardo, A. S., Rodrigues, R. F., Martins, R. C., Castro, L. M., & Quinta-Ferreira, R. M. (2015). Phenolic wastewaters treatment by electrocoagulation process using Zn anode. Chemical Engineering Journal, 275, 331-341.

Instituto Superior de Engenharia
Politécnico de Coimbra